João Marcus Soares Callegari

# Lifetime Evaluation of Three-Phase Multifunctional PV Inverters with Reactive Power Compensation

Viçosa

2018

João Marcus Soares Callegari

# Lifetime Evaluation of Three-Phase Multifunctional PV Inverters with Reactive Power Compensation

Monografia apresentada ao Departamento de Engenharia Elétrica do Centro de Ciências Exatas e Tecnológicas da Universidade Federal de Viçosa, para a obtenção dos créditos da disciplina ELT 490 - Monografia e Seminário e cumprimento do requisito parcial para obtenção do grau de Bacharel em Engenharia Elétrica.

Universidade Federal de Viçosa

Departamento de Engenharia Elétrica

Curso de Graduação em Engenharia Elétrica

Orientador: Heverton Augusto Pereira

Coorientador: Erick Matheus da Silveira Brito

Viçosa

2018

**JOÃO MARCUS SOARES CALLEGARI**

# LIFETIME EVALUATION OF THREE-PHASE MULTIFUNCTIONAL PV INVERTERS WITH REACTIVE POWER COMPENSATION

Monografia apresentada ao Departamento de Engenharia Elétrica do Centro de Ciências Exatas e Tecnológicas da Universidade Federal de Viçosa, para a obtenção dos créditos da disciplina ELT 490 – Monografia e Seminário e cumprimento do requisito parcial para obtenção do grau de Bacharel em Engenharia Elétrica.

Trabalho aprovado em 19 de outubro de 2018.

COMISSÃO EXAMINADORA

Prof. Dr. Heverton Augusto Pereira – Orientador
Universidade Federal de Viçosa - UFV

Prof. M. Sc.. Erick Matheus da Silveira Brito – Co-orientador
Universidade Federal de Minas Gerais - UFMG

Prof. M. Sc.. Allan Fagner Cupertino – Membro Externo
Centro Federal de Educação Tecnológica – CEFET-MG

Dr. Ariya Sangwongwanich – Membro Externo
Aalborg University

VIÇOSA, MG
2018

*À minha família, mentores e amigos.*

# Agradecimentos

Ao longo desta caminhada, muitas pessoas me ajudaram de diversas maneiras. Isto não é nenhum exagero: este trabalho jamais teria sido possível sem o apoio de cada uma delas, a quem sou extremamente grato.

Em primeiro lugar, não posso deixar de agradecer a Deus, por me conceder a força necessária para superar os desafios impostos durante a execução deste trabalho. Obrigado por me iluminar nesta longa batalha.

Agradeço profundamente aos meus pais, Magda e Marcus, pelo incentivo, amor, confiança e apoio durante toda minha vida acadêmica. Vocês construiram uma base sólida para que eu pudesse me apoiar durante quaisquer percalços que tive de enfrentar e sempre estiveram presentes para me mostrar qual a melhor escolha. Aprendi com vocês a importância da dedicação para evolução pessoal.

O meu muito obrigado aos meus irmãos, Luís Filipe e Pedro Paulo, que sempre se preocuparam com o meu bem estar. Fizeram os meus dias melhores, seja por ligação, seja por mensagem. Deixo registrado a minha eterna gratidão.

Ao meu avô, meu maior exemplo, por todos os conselhos e conversas. Obrigado pela amizade, pelas nossas caminhadas, pelos ensinamentos e pela paciência em me escutar durante meus instantes de desânimo.

Agradeço também o apoio que recebi dos meus familiares, em especial à minha madrinha e tio, Maria Aparecida e Sebastião, por acreditarem em mim nos momentos em que não me julguei capaz.

Agradeço à minha namorada, Bia, um anjo que caiu de paraquedas na minha vida. Sua presença se fez necessária em cada momento, como fonte de carinho, segurança e gratidão. Saiba que minhas vitórias são graças a você, que nunca exitou em me auxiliar, esteve presente em todos os momentos adversos e sempre soube lidar em qualquer situação.

Yole, minha tia-avó, esteve atuando ativamente na minha formação, desde as minhas primeiras palavras. Compartilhou comigo, nos últimos anos de sua vida, um de seus maiores sonhos: vivenciar o crescimento acadêmico de seus netos. Acredito estar trilhando o caminho, no qual sonhou para nós, netos. À ela, sou imensamente grato por todos os nossos momentos e pela motivação de buscar os meus sonhos.

À Universidade Federal de Viçosa (UFV) e ao corpo docente do Departamento de Engenharia Elétrica pela oportunidade de aprimorar meus conhecimentos e por todo apoio fornecido. Agradeço ao GESEP por todo suporte prestado durante o desenvolvimento deste trabalho, em especial ao meu orientador prof. Heverton e coorientador prof. Erick.

Seus conhecimentos e competência puderam sanar minhas dúvidas.

Desejo igualmente agradecer a todos os meus colegas e amigos da graduação, do GESEP e Casa Amarela, especialmente o William, Lucas, Paulo, Matheus e Dayane, cujo apoio e amizade estiveram presentes em todos os momentos.

*"A mente que se abre a uma nova ideia*
*jamais voltará ao seu tamanho original."*
*(Albert Einstein)*

# Resumo

A operação multifuncional de inversores fotovoltaicos consiste em fornecer serviços auxiliares à rede, como injeção de potência reativa, compensação de correntes harmônicas, regulação de frequência e outros. Uma vez que os inversores fotovoltaicos são normalmente projetados para operar sob condições de carga parcial, isto é, possuem margem de corrente não explorada, eles podem auxiliar a rede elétrica com injeção de potência reativa durante operação de baixo carregamento para melhorar a qualidade de energia elétrica, auxiliar na regulação de tensão e fator de potência. No entanto, essa atividade extra pode causar estresse térmico nos componentes do inversor fotovoltaico, afetando sua confiabilidade. Para medir a influência da injeção de potência reativa na vida útil do inversor, utiliza-se um modelo térmico para estimar a temperatura da junção dos dispositivos de potência e um modelo estatístico de vida útil para avaliar o consumo de vida útil do sistema. Por fim, uma análise estatística simula vários cenários de operação dos dispositivos de potência, para os casos com e sem injeção de potência reativa. Este trabalho analisa a vida útil dos inversores PV considerando a injeção de potência reativa baseada em um perfil de carga real, comparado à operação tradicional do inversor. A avaliação foi realizada em um sistema fotovoltaico, considerando perfis de irradiância e temperatura da Dinamarca. Os resultados mostram que a injeção de potência reativa tem um impacto considerável na confiabilidade do inversor PV, reduzindo em 3 vezes a estimativa da vida útil quando este serviço é realizado.

**Palavras-chaves**: Sistema fotovoltaico; Inversor fotovoltaico multifuncional; injeção de potência reativa; confiabilidade; vida útil; confiabilidade no nível do componente; confiabilidade no nível do sistema.

# Abstract

The multifunctional operation of photovoltaic (PV) inverters consists of providing ancillary services into the grid, such as reactive power injection, harmonic current compensation, frequency regulation and others. Once PV inverters are usually designed to operate under partial load conditions for daily operations, i.e., the inverter has a current margin which is not explored, they can assist the main grid with reactive power injection during low load operation in order to improve the grid quality, assist in voltage regulation and power factor. However, this extra activity can cause thermal stress in the PV inverter components, affecting their reliability. In order to measure the influence of the reactive power injection, an equivalent thermal model is used to estimate the junction temperature of the power devices and a lifetime model is used to evaluate the system reliability. Finally, it is simulated several operation scenarios of the power devices, and statistical analysis are performed for the cases with and without reactive power injection. Therefore, this work analyzes lifetime of the PV inverters, considering the reactive power injection based on a real load profile, compared to a traditional inverter operation. The evaluation has been carried out on the PV system, considering the irradiance and ambient temperature profiles from Denmark. The results show that the reactive power injection has a considerable impact on the reliability of the PV inverter, reducing by 3 times the lifetime estimation when this service is performed.

**Key-words**: PV system; Multifunctional PV inverter; reactive power injection; reliability; lifetime; component-level reliability; system-level reliability.

# List of Figures


Figure 1 – Solar PV global capacity and annual additions, from 2007 to 2017. Adapted from (REN21, 2018). . . . . 19
Figure 2 – Main features of the multifunctional PV inverter. . . . . 20
Figure 3 – Operation curve of a real PV inverter during a measurement day. (b) Available operation area for ancillary services. . . . . 21
Figure 4 – Structure of a three-phase grid-connected PV system. . . . . 24
Figure 5 – (a) Structure of PV system studied, with the measured variables to implement the PV inverter control. (b) Block diagram of control strategy. 25
Figure 6 – (a) SRF-PLL block diagram. (b) Linearized SRF-PLL block diagram of (2.3). . . . . 26
Figure 7 – (a) $Q$ control block diagram. (b) $Q$ control simplified block diagram. . 28
Figure 8 – (a) Zero sequence signal calculator ($v_0$) to be added into the reference. (b) Signal block diagram of the SVPWM employing the zero-sequence injection principle. . . . . 30
Figure 9 – (a) Typical input waveforms of the SVPWM modulator. (b) IGBT gate signals. (c) Zoom of the $v_0$, $v_{ga}^*$ and the sum of $v_0$ and $v_{ga}^*$. . . . . 31
Figure 10 – Flowchart of IGBT physics failure types. . . . . 31
Figure 11 – Phase current injected into the grid with and without reactive power injection. . . . . 35
Figure 12 – The characteristic curves: (a) $v_f$ x $i_f$ of the diode, (b) $v_{ce}$ x $i_c$ of the IGBT and the linear approximation for both. . . . . 36
Figure 13 – Collector currents $i_c$ of IGBTs S1 and S2. Zoom in the typical waveforms of switching and conduction current of IGBT S1. . . . . 38
Figure 14 – Analysis of (a) conduction power losses, and (b) switching power losses, for variations of $\theta$ from $-\pi$ to $\pi$ and $S_{base} = 8$ kVA. . . . . 40
Figure 15 – Structure of a standard IGBT module. . . . . 41
Figure 16 – Thermal (a) Cauer-model. (b) Foster-model. . . . . 42
Figure 17 – Mission profile of: (a) Solar irradiance 1-year profile. (b) Ambient temperature 1-year profile. (c) Reactive power injection 1-year profile, according to the load requirement. (d) Zoom of reactive power injection 1-week profile. . . . . 43
Figure 18 – Flowchart for the lifetime evaluation of power devices. . . . . 44
Figure 19 – Thermal model to estimate junction temperature. Adapted from (MA et al., 2015). . . . . 45
Figure 20 – Thermal cycling due to the grid frequency (index $s$) and due to climatic variations (index $l$). . . . . 46

Figure 21 – (a) Real pulsed power losses and two steps power losses pulses approximation. (b) Junction temperature corresponding to the two-pulses approximation and real junction temperature. . . . . 47
Figure 22 – Flowchart of the Monte Carlo reliability analysis. . . . . 49
Figure 23 – Power losses in the semiconductors devices considering different injections of active and reactive power. Diode: (a) conduction losses, (b) switching losses, (c) total losses. IGBT: (d) conduction losses, (e) switching losses, (f) total losses. . . . . 53
Figure 24 – (a) IGBT junction temperature behavior with and without $Q$ injection. (b) IGBT junction temperature fluctuation with and without $Q$ injection. (c) Diode junction temperature behavior with and without $Q$ injection. (d) Diode junction temperature fluctuation with and without $Q$ injection. 54
Figure 25 – Damage distribution analysis of the power module with and without Q injection. Unreliability function of the PV inverter (b) without $Q$ compensation; (c) with $Q$ compensation. . . . . 56
Figure 26 – Unreliability function of the PV inverter (a) without $Q$ compensation; (b) with $Q$ compensation. . . . . 56
Figure 27 – (a) Typical IGBT turn on curve. (b) Linearized approximation. . . . . 66
Figure 28 – (a) Typical IGBT turn off curve. (b) Linearized approximation. . . . . 68

# List of Tables

Table 1 – Typical values of the parameters from power losses equations found in the IGBTs and diodes datasheets. . . . . 39
Table 2 – Foster thermal impedance for IKW25T120 power module from Infineon. 43
Table 3 – Parameters and limits for the calculation of $N_f$ based on the Bayerer Model after the correction (REIGOSA, 2014). . . . . 48
Table 4 – Parameters of the PV system. . . . . 52
Table 5 – Controllers gains. . . . . 53
Table 6 – Lifetime consumption due $T_a$, $G$ and $Q$ profiles, based on the Palmgren-Miner's rule (3.22) for one year. . . . . 55

# List of abbreviations and acronyms

| | |
|---|---|
| PV | Photovoltaic |
| IEEE | Institute of Electrical and Electronics Engineers |
| IEC | International Electrotechnical Commission |
| d.c | Direct Current |
| a.c | Alternating Current |
| EPS | Electric Power System |
| PF | Power Factor |
| Q | Reactive Power |
| IGBT | Insulated Gate Bipolar Transistor |
| PWM | Pulse Width Modulation |
| SVPWM | Space Vector PWM |
| SPWM | Sinusoidal PWM |
| dq | Synchronous Reference Frame |
| PLL | Phase-Locked Loop |
| d | Direct grid component |
| q | Quadrature grid component |
| SRF-PLL | Synchronous Reference Frame PLL |
| TF | Transfer function |
| P | Active power |
| PoF | Physics-of-Failure |
| Al | Aluminum |
| Si | Silicon |
| PCC | Point of common coupling |

| | |
|---|---|
| DCB | Direct copper-bonded |
| LC | Lifetime consumption |
| PDF | Probability Density Function |
| CDF | Cumulative Density Function |
| SiC | Silicon Carbide |

# List of symbols

| | |
|---|---|
| $L_f$ | Filter inductance (Inverter side) |
| $L_g$ | Filter inductance (Grid side) |
| $C_f$ | Filter capacitance |
| $r_d$ | Filter damping resistor |
| $f_n$ | Nominal grid frequency |
| $f_{sw}$ | Switching frequency |
| $v_{dc}$ | dc-link voltage |
| $v_0$ | Zero sequence signal |
| $v_{ga}^*$ | Reference signal of phase $a$ |
| $v_{gb}^*$ | Reference signal of phase $b$ |
| $v_{gc}^*$ | Reference signal of phase $c$ |
| $v_{gabc}$ | Three-phase voltage in natural reference frame |
| $\omega_n$ | Fundamental angular frequency |
| $\theta_0$ | Initial phase angle of the grid |
| $\rho$ | Tracked angle |
| $G_{PLL}$ | PLL: PI controller |
| $k_{p1}$ | PLL: Proportional gain |
| $k_{i1}$ | PLL: Integral gain |
| $\tau_1$ | PLL: Constant time gain |
| $\omega_{nt}$ | Natural frequency |
| $\xi$ | Damping coefficient |
| $v_{gq}$ | Quadrature grid voltage component |
| $v_{gd}$ | Direct grid voltage component |

| | |
|---|---|
| $i_{gd}$ | Direct grid current component |
| $i_{gq}$ | Quadrature grid current component |
| $G_Q$ | Q: PI controller |
| $k_{p,Q}$ | Q: Proportional gain |
| $k_{i,Q}$ | Q: Integral gain |
| $N_f$ | Number of cycles to failure |
| $\Delta T_j$ | Junction temperature fluctuation |
| $k_b$ | Boltzmann constant |
| $E_a$ | Activation energy |
| $I$ | Current per bond foot |
| $V$ | Blocking voltage |
| $D$ | Bond wire diameter |
| $t_{on}$ | Cycle heating time |
| $T_{jm}$ | Average junction temperature |
| $S$ | Apparent power |
| $I_g$ | $rms$ values of the grid current |
| $V_g$ | $rms$ values of the grid voltage |
| $P_{tot}$ | Total power losses |
| $P_c$ | Conduction power losses |
| $P_{sw}$ | Switching power losses |
| $i_{ga}$ | Instantaneous current of the phase $a$ |
| $v_{ga}$ | Instantaneous voltage of the phase $a$ |
| $V_{cm}$ | Phase voltage amplitude |
| $I_{cm}$ | Phase current amplitude |
| $v_{ce}$ | IGBT collector-emitter voltage |
| $i_c$ | IGBT collector current |

| | |
|---|---|
| $v_f$ | Diode forward voltage |
| $i_f$ | Diode forward current |
| $V_{cen}$ | IGBT collector-emitter voltage for rated operating condition |
| $V_{ce0}$ | IGBT on-state zero current collector-emitter voltage |
| $V_{fn}$ | Forward diode voltage for rated condition |
| $V_{f0}$ | On-state zero current voltage across the diode |
| $I_{cn}$ | Rated collector current |
| $r_i$ | IGBT collector-emitter on-state resistance |
| $r_{di}$ | Diode on-state resistance |
| $h$ | Modulation function |
| $\delta$ | Duty cycle |
| $m$ | Modulation index |
| $P_{c,I}$ | IGBT conduction losses |
| $P_{c,D}$ | Diode conduction losses |
| $\theta$ | Angle between the current and voltage waveforms |
| $P_{on,I}$ | IGBT on-state average switching power losses |
| $P_{off,I}$ | IGBT off-state average switching power losses |
| $P_{off,D}$ | Diode off-state average switching power losses |
| $t_{rn}$ | Rated IGBT current rise time |
| $t_{rrn}$ | Diode nominal reverse recovery time |
| $Q_{rrn}$ | Nominal reverse diode recovery load |
| $t_{fn}$ | Rated IGBT current fall time |
| $Z_{th_{jc}}$ | Transient thermal impedance between the junction of the IGBT/diode chips and the case module |
| $Z_{th_{ch}}$ | Thermal impedance between case module and heatsink |
| $Z_{th_{ha}}$ | Transient thermal impedance between heatsink and ambient |

| | |
|---|---|
| $T_j$ | Junction temperature |
| $T_c$ | Case temperature |
| $R_{(jc)}$ | Junction to case thermal resistance |
| $C_{(jc)}$ | Junction to case thermal capacitance |
| $\tau$ | Thermal time constant |
| $G$ | Solar irradiance |
| $T_a$ | Ambient temperature |
| $P_{in}$ | Active input power on the PV inverter, produced in the PV panels |
| $t_{on(l)}$ | Long-term cycle heating time |
| $T_{jm(l)}$ | Long-term average junction temperature |
| $\Delta T_{j(l)}$ | Long-term junction temperature fluctuation |
| $t_{on(s)}$ | Short-term cycle heating time |
| $T_{jm(s)}$ | Short-term average junction temperature |
| $\Delta T_{j(s)}$ | Short-term junction temperature fluctuation |
| $Z_{th}$ | Time-based expression of device thermal impedance |
| $P_{I,tot}$ | IGBT total power losses |
| $t_{on}^{'}$ | Equivalent static $t_{on}$ |
| $T_{jm}^{'}$ | Equivalent static $T_{jm}$ |
| $\Delta T_{j}^{'}$ | Equivalent static $\Delta T_j$ |
| $NC^{'}$ | Number of cycles per year |
| $N_{f}^{'}$ | Equivalent number of cycles to failure per year |
| $f(x)$ | Weibull PDF |
| $x$ | Operation time |
| $F(x)$ | Weibull CDF; or component unreliability function |
| $B_{10}$ | Time when 10 % of samples have failed |
| $F_{sys}(x)$ | System unreliability function |

# Contents


**1 INTRODUCTION . . . . . 19**
**1.1 Motivation and Problematic . . . . . 21**
**1.2 Contributions and Objectives . . . . . 22**

**2 LITERATURE REVIEW . . . . . 24**
**2.1 Grid-connected Three Phase PV Inverter . . . . . 24**
**2.2 Control Strategy . . . . . 25**
2.2.1 SRF-PLL . . . . . 26
2.2.2 Active and Reactive Power Injection Control . . . . . 27
2.2.3 Modulation Strategy . . . . . 29
**2.3 Physics-of-Failure of IGBT Modules . . . . . 30**
**2.4 Lifetime Models . . . . . 32**
2.4.1 Coffin-Manson Model . . . . . 33
2.4.2 Coffin-Manson-Arrhenius Model . . . . . 33
2.4.3 Coffin-Manson-Arrhenius-Landzberg Model . . . . . 33
2.4.4 Bayerer Model . . . . . 33
**2.5 Reactive Power as Ancillary Service of the Multifunctional PV Inverter . . . . . 34**

**3 METHODOLOGY . . . . . 35**
**3.1 Power Losses Analysis in Electronics Devices with Reactive Power Injection . . . . . 35**
3.1.1 Analytical Mathematical Model of Conduction Power Losses . . . . . 37
3.1.2 Analytical Mathematical Model of Switching Power Losses . . . . . 38
**3.2 Thermal Modeling of PV Inverter . . . . . 41**
3.2.1 Thermal Equivalent Circuit Models . . . . . 42
**3.3 Lifetime Evaluation Procedure . . . . . 43**
3.3.1 Electro-Thermal Hybrid Model . . . . . 44
3.3.2 Lifetime Evaluation for Different Time Constants . . . . . 45
3.3.3 Lifetime Consumption Evaluation . . . . . 49
**3.4 Monte Carlo Reliability Analysis . . . . . 49**

**4 RESULTS AND DISCUSSION . . . . . 52**
**4.1 Case Study . . . . . 52**
**4.2 Total LC based on Mission Profile . . . . . 53**

**5 CONCLUSION . . . . . 58**
**5.1 Final Considerations . . . . . 58**
**5.2 Continuity Proposals . . . . . 59**

**REFERENCES . . . . . 61**

**APPENDIX A – SWITCHING POWER LOSSES MODELING . . . . 66**
**A.1 IGBT Switching Power Losses Modeling . . . . . 66**
A.1.1 Turn on Switching Power Losses . . . . . 66
A.1.2 Turn off Switching Power Losses . . . . . 68
**A.2 Diode Switching Power Losses Modeling . . . . . 69**

# 1 Introduction

Electric energy is essential for maintaining the modern man's lifestyle. Much of the electricity generation is carried out based on non-renewable resources. However, the limitation of natural reserves, the environmental impact and the increase in the price associated with fossil fuels indicates the need for a diversification in the energy matrix. These factors motivate researches in the renewable sources fields, such as solar, wind and biomass energy (GANGOPADHYAY; JANA; DAS, 2013).

Photovoltaic (PV) solar energy has experienced one of the largest growths in recent decades, among renewable energy sources. Renewable energy contributed with almost two-thirds of new power capacity around the world in 2016 (165 GW), being 76 GW of contribution of PV solar energy (AGENCY, 2018). In this scenario, the solar PV capacity grew by 25% in 2017, reaching over 98 GW installed, for a cumulative total of approximately 402 GW. On average, the equivalent of more than 40,000 solar panels was installed each hour of the year (REN21, 2018). For the first time, the solar PV technology rose faster than any other source, surpassing the coal net growth.

Solar PV global capacity in 10 years grew from 8 GW to 402 GW, an increase of approximately 50 times, as shown in Fig. 1. This same figure illustrates the annual addition, in GW, of this new technology in the power system.

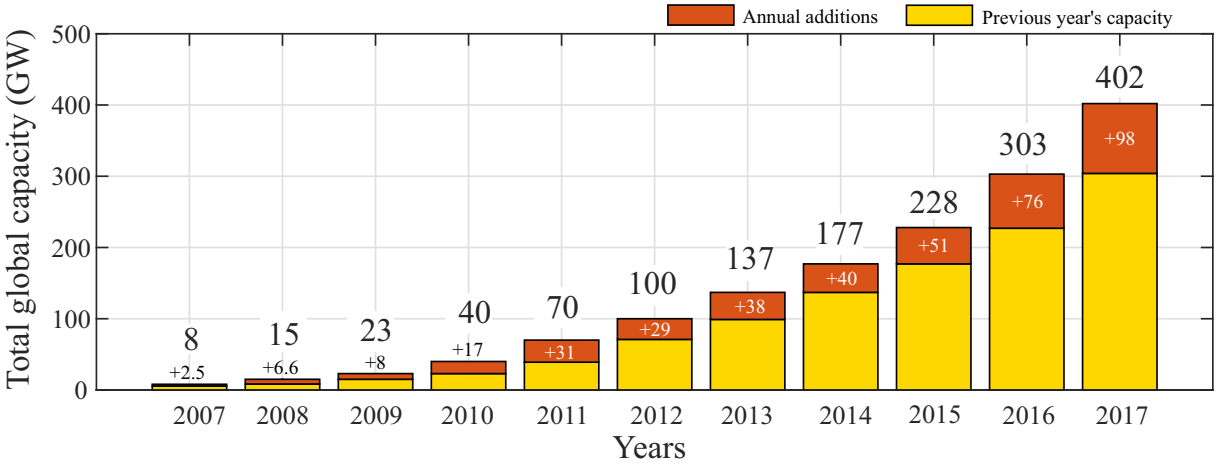


Figure 1 – Solar PV global capacity and annual additions, from 2007 to 2017. Adapted from (REN21, 2018).

This scenario is directly related to reduced costs, increases in investment and advances in PV technology (GAO et al., 2016; MAYER, 2015). Therefore, the PV systems became a reality in the current energy market, with great potential to become one of the major energy sources in the near future (SANGWONGWANICH et al., 2018; JäGER-

WALDAU, 2017). PV systems became very attractive to produce sustainable electricity for diversified purposes. Besides, these systems present lower environmental impacts and reduced maintenance costs (ANDRADE et al., 2016; ANURAG; YANG; BLAABJERG, 2015b; LIBO; ZHENGMING; JIANZHENG, 2007).

The PV systems can operate in grid-tied or off-grid configuration. For the first option, some international standards define technical requirements, such as IEEE 1547, IEEE 929-2000 and IEC 61727 (ALMEIDA, 2011). The standard ABNT NBR 16149 is the one that regulates the characteristics for connection of PV systems to the grid in Brazil.

The PV inverter is the component responsible for converting the direct current (d.c) generated by the PV panels in alternating current (a.c) to inject into the grid. The increasing penetration of PV systems (stochastic and intermittent renewable energy source) into the grid has made it more vulnerable, decentralized and susceptible to disturbances, which has led to the conductance of studies on their connection impacts (REIGOSA, 2014). Moreover, with the advancement of the technology, the electric loads fed by the grid have become non-linear, increasing the harmonic content in the Electric Power System (EPS) (ZENG et al., 2015). Therefore, the harmonic and reactive current flowing in the grid can cause extra power losses, vibration and noise in the electric machines and transformers.

In order to improve grid power quality, an interesting solution is to make some changes in the philosophy of PV systems operation and control. In this context, some works in the literature proposed the multifunctional use of inverters. This concept proposes additions in the inverter control algorithm to provide ancillary services, such as reactive power ($Q$) support, harmonic current compensation and others (LIU et al., 2015; PEREIRA et al., 2015). Fig. 2 shows the main multifunctional features of the PV inverter currently studied, focusing on the reactive power support advantages: voltage regulation at steady state and transient state, reduction of power losses in transmission lines due to the supply of reactive power near loads and power factor regulation.

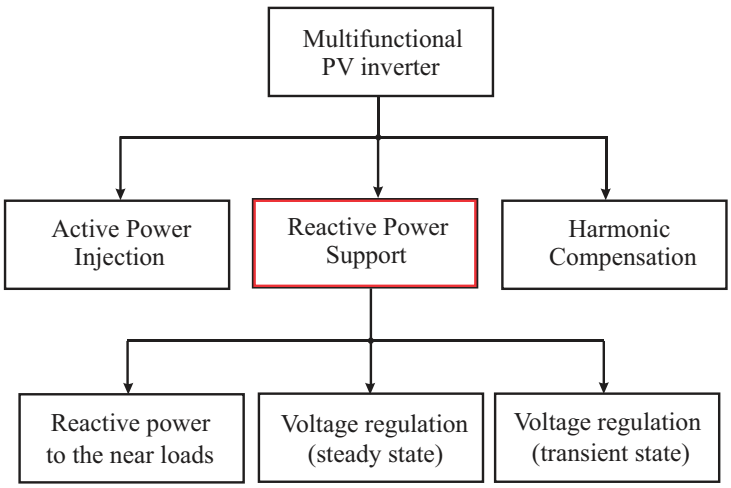


Figure 2 – Main features of the multifunctional PV inverter.

Once PV inverters are usually designed to operate under partial load conditions for daily operations, i.e., the inverter has a current margin which is not explored, they can assist the main grid with reactive power injection during low load operation, e.g. at night or during low solar irradiance profile. Fig. 3(a) shows an operation curve of a real PV inverter during a typical sunny day. The operation curve does not exceed 30% of the total operation area. Thereby, it remains an area of 70%, which can be used for ancillary services, as shown in Fig. 3(b). Improving the grid power quality is one of the reasons for the growing interest of the use the multifunctional PV inverters.

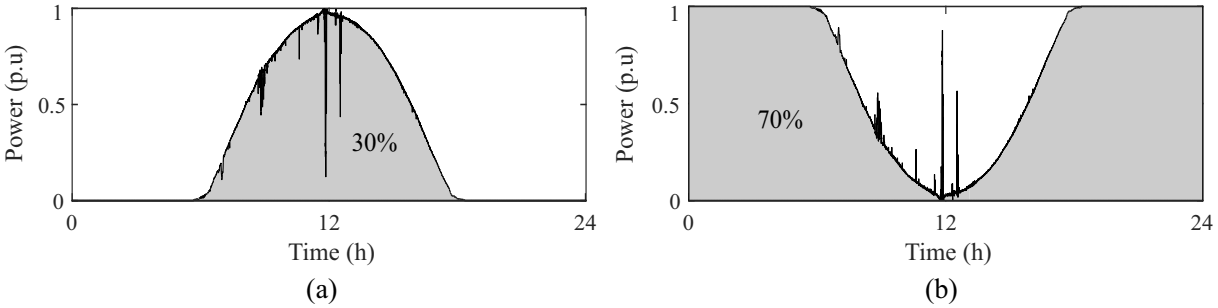


Figure 3 – Operation curve of a real PV inverter during a measurement day. (b) Available operation area for ancillary services.

## 1.1 Motivation and Problematic

An important issue involving the impacts of the connection of PV systems to the grid is the reduction of the power factor (PF) of the consumer units because they produce their own active power demand. In this case, the load reactive power is only supplied by the grid or by the addition of extra capacitor banks. Therefore, according to the grid code requirements, the reduction of PF implies the application of fees by the electric utility, which reduces the economic advantage of PV systems (PINTO; ZILLES, 2014). Currently, two conventional techniques are used to solve this problem: synchronous machines and capacitor banks. The former provides reactive power to the system, when overexcited. It is economically viable in operations involving loads greater than 200 HP. Alternatively, the latter is used for localized reactive power compensation. However, switching a capacitor bank during a transient instability may not be fast enough to prevent damages to the system (SARKAR; MEEGAHAPOLA; DATTA, 2018). These limitations suggest the need for a new approach, so as to improve flexibility and reduce costs.

Recently, the multifunctional PV inverter presents itself as a solution with high effectiveness for the aforementioned limitations, since its control of the reactive power injection allows the inverter to realize the PF correction and consequently the grid voltage regulation. Nevertheless, this imply in a additional use of PV inverters and some impact is expected in the PV inverters lifetime.

Previous studies show that PV inverters are among the least reliable components of PV plants (KAPLAR et al., 2011). About 32% of the inverter failures occur in the power semiconductors (REIGOSA, 2014). In addition, the manufacturers of PV modules guarantee lifetime over 20 years, while the typical guarantee period for PV inverters range from 5 to 10 years (FERREIRA et al., 2017). Since the inverter will be operating on a previously unexploited feature, an adequate assessment of reliability performance for the multifunctional inverter is crucial to infer whether this new functionality is interesting from the lifetime point of view, compared to the traditional inverter. Indeed, the extra work-time with reactive power compensation during low irradiation profiles can causes additional thermal stress and decreasing the inverter efficiency (MURAY; DAVOUDI; CHAPMAN, 2011; ANURAG; YANG; BLAABJERG, 2015a).

## 1.2 Contributions and Objectives

Currently, studies on the multifunctional inverter have risen great interest from academic researches, mainly regarding the design and control areas. For example, (ZHANG et al., 2014) discusses the thermal control technique of the power device by means of the reactive power that circulates between parallel converters, improving devices reliability. (GANDHI et al., 2018) studies the effects of reactive power injection from PV inverters on their lifetime. Besides, the author translates the reduction in inverter lifetime due to reactive power injection into reactive power cost for PV system. The impact of PV module characteristic on the reliability and lifetime of PV inverters is approached by (SANGWONGWANICH; LIIVIK; BLAABJERG, 2018). On the other hand, (ANURAG; YANG; BLAABJERG, 2015a) analyzes the reliability based on a long-term thermal loading of the PV inverter with different values of $Q$ injection at night.

Despite the efforts of multifunctional PV inverter researchers, few works in literature analyze the effect of thermal stress on power modules, when the PV inverter injects reactive power. Furthermore, the reactive power profiles considered in these works are theoretical. The industries are interested in evaluating the impacts of reactive power injection according to a real profile, which has not been investigated yet. Thus, this work aims to fulfill this void in the literature, presenting a study on inverter lifetime when a real reactive profile obtained from an industry is injected. Therefore, this work provides the following contributions:

- Reactive power compensation according to a real $Q$ profile;
- Influence of thermal cycles due to climatic variations (measured solar irradiance and ambient temperature profiles) and grid frequency in the multifunctional inverter lifetime;

- Lifetime analysis with the Monte-Carlo simulation for $Q$ injection in comparison with the conventional operation.

Besides, this work aims to achieve the following objectives:

- Present a simplified analytical model for the conduction and switching power losses of the PV inverter power devices, injecting $Q$;
- Design and simulate a three-phase two-level PV inverter;
- Electro-thermal model description for the power modules;
- Compare lifetime prediction with and without reactive power compensation.

This work is divided in five chapters. In this first chapter was presented the contextualization, the motivation, objectives and their contributions.

For the other chapters, this work is outlined as follows: Chapter 2 provides a literature review with the multifunctional PV inverter control and design, i.e, description of the modeling control strategy implemented to regulate the active and reactive power flow. Besides, the failures types in the inverter critical elements (power modules) and lifetime models are briefly presented.

Chapter 3 shows the methodology to study the lifetime analysis of the three-phase grid-connected PV inverter power devices. The influence of the PF angle variation on the conduction and switching power losses is also evaluated. In addition, this chapter describes the equivalent thermal model used in the lifetime evaluation, it is also quantifies accumulated damage in the power module over one year and introduces the effect of parameter variation in PV inverter reliability by means of Monte Carlo simulation.

Chapter 4 presents a case study with and without reactive power compensation, determining the lifetime consumption as a result. Finally, conclusions are stated in Chapter 5, as well as the proposals for continuity of this work.

# 2 Literature Review

In this chapter, a theoretical review of the most relevant multifunctional PV inverter concepts, design, control strategy and modulation, are presented.

## 2.1 Grid-connected Three Phase PV Inverter

The PV system considered in this work has a grid-connected three phase configuration, as shown in Fig. 4. The PV inverter is a d.c-a.c converter responsible for transforming the energy produced by PV panels, due to solar irradiance, in alternating energy. It consists of six (6) Insulated Gate Bipolar Transistor (IGBT) semiconductor devices and six (6) anti-parallel Diodes.

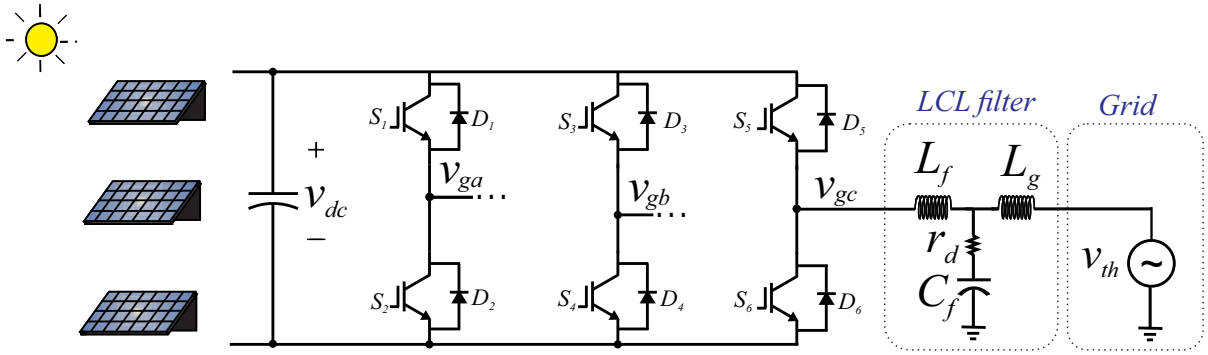


Figure 4 – Structure of a three-phase grid-connected PV system.

The IGBTs in the same phase are activated in a complementary way. For example, S1 is on-state when S2 is not activated and vice-verse. This analysis is analogous to the other phases, i.e., S3 and S4, as well as S5 and S6.

Voltage and current harmonics are generated at the output of the inverter due to the power devices switching characteristics (ZOU; WANG; CHENG, 2014; ANURAG; YANG; BLAABJERG, 2015a). Thus, the use of a passive filter is necessary to mitigate the circulation of these undesirable components to the grid. As shown in Fig. 4, the LCL filter has two inductors ($L_f$ and $L_g$) and one capacitor ($C_f$). It has less bulky inductors than the $L$ filter and it has an attenuation of 60 dB/dec (3rd order filter) after the resonance peak. In addition, the $L_g$ inductance reduces transients from the inverter connection to the grid.

During the design of the LCL filter, special care must be taken for its resonant frequency, since it tends to destabilize the inverter control (LISERRE; BLAABJERG; HANSEN, 2005). Besides, damping techniques for the purpose of damping the filter resonance must be implemented. Inserting the resistor $r_d$ in series with the filter capacitor

provides passive damping. Increasing $r_d$ reduces the filter resonant peak, but reduces the filter attenuation at high frequencies and increases power losses (GOMES; CUPERTINO; PEREIRA, 2018). These factors require a cost-benefit ratio in the LCL filters with passive damping design. Finally, the design methodology of the LCL filter is in agreement with (PEñA-ALZOLA et al., 2014; GOMES; CUPERTINO; PEREIRA, 2018).

## 2.2 Control Strategy

The control algorithm is implemented in synchronous reference frame ($dq$). The three-phase voltage vector $v_{gabc}$, shown in Fig. 5(a), is translated from the natural reference frame $abc$ to the rotating reference frame $dq$ by using Park's transformation (RODRIGUEZ et al., 2007). More details can be found in (TEIXEIRA, 2010; ALMEIDA, 2011).

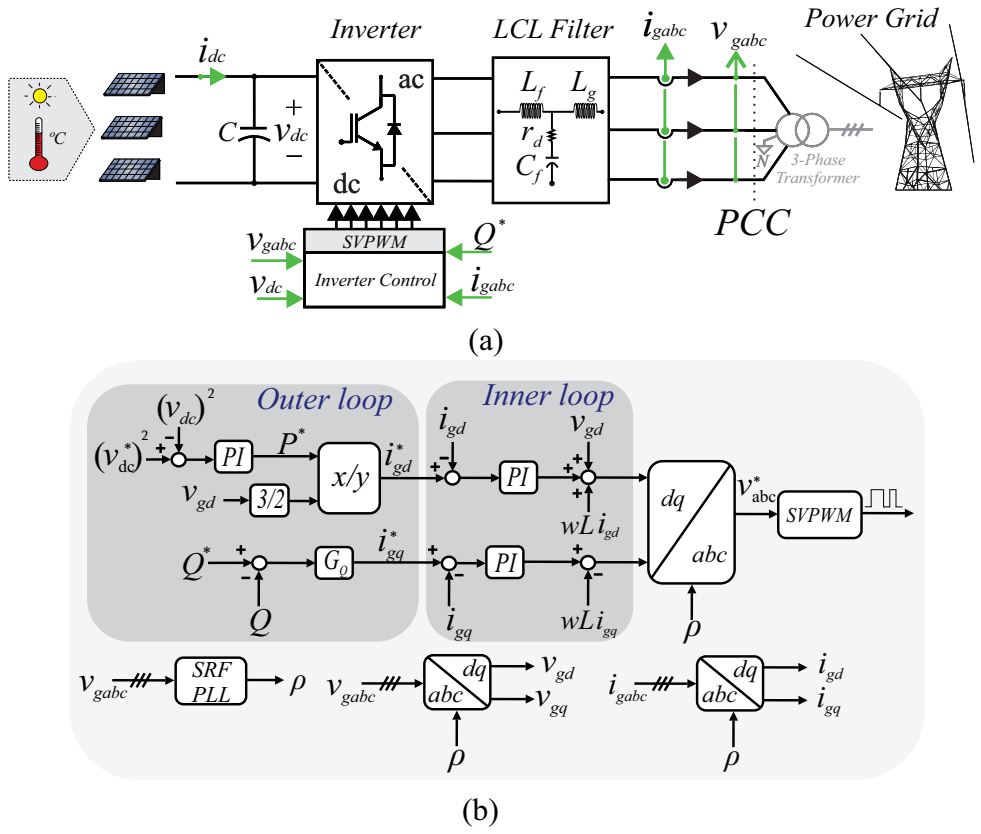


Figure 5 – (a) Structure of PV system studied, with the measured variables to implement the PV inverter control. (b) Block diagram of control strategy.

The control strategy is developed in two cascade loops, as shown in Fig. 5(b). The inner loop has a faster dynamic response and controls the current injected by the inverter. The outer loop is slower and controls the inverter input voltage in the dc-link and the reactive power injected into the grid (XAVIER; CUPERTINO; PEREIRA, 2018).

In order to guarantee the synchronization of the $dq$ control with the grid, it is necessary to accurately measure the angular frequency and the phase angle by means of a

Phase-Locked Loop (PLL).

### 2.2.1 SRF-PLL

A Synchronous Reference Frame Phase-Locked Loop (SRF-PLL) structure is used to synchronize the inverter output to the grid (GOLESTAN; GUERRERO; VASQUEZ, 2017), based on $dq$ coordinates.

For a balanced three-phase system, the direct ($d$) and quadrature ($q$) grid components are determined by the Park's transformation, whose result is:

$$\begin{cases} v_{gd} = V_m cos(w_n t + \theta_0 - \rho(t)) \\ v_{gq} = V_m sin(w_n t + \theta_0 - \rho(t)), \end{cases} \tag{2.1}$$

where $V_m$ is the amplitude in Volts, $w_n$ is the fundamental angular frequency (rad/s), $\theta_0$ is the initial phase angle of the grid (rad) and $\rho$ is the tracked angle.

Fig. 6 shows the block diagram of the SRF-PLL. If $\rho = w_n t + \theta_0$, $v_{gd} = V_m$ and $v_{gq} = 0$. Therefore, it is possible to design a PI controller to cancel $v_{gq}$ in steady-state.

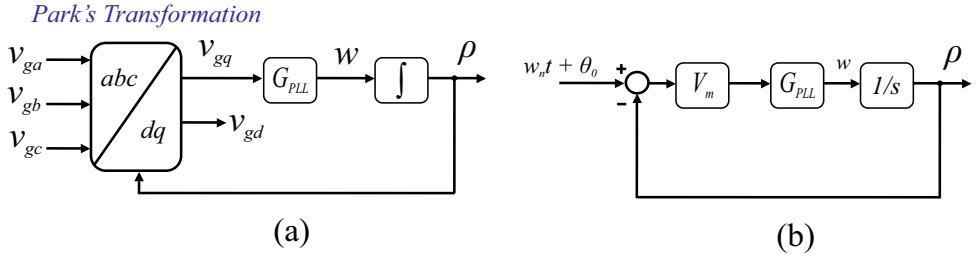


Figure 6 – (a) SRF-PLL block diagram. (b) Linearized SRF-PLL block diagram of (2.3).

From Fig. 6, it is possible to observe:

$$w = \frac{d\rho}{dt} = v_{gq} G_{PLL} = V_m sin(w_n t + \theta_0 - \rho(t)) G_{PLL}. \tag{2.2}$$

A nonlinear dynamics of the synchronization circuit is observed. However, the argument of the sinusoidal function is very small in steady state, since $\rho \cong w_n t + \theta_0$. Thus, it is possible to linearize $sin(w_n t + \theta_0 - \rho(t))$ by $(w_n t + \theta_0 - \rho(t))$, as:

$$w = \frac{d\rho}{dt} \cong V_m (w_n t + \theta_0 - \rho(t)) G_{PLL}. \tag{2.3}$$

The above equation is described by the block diagram of Fig. 6(b) and its closed loop transfer function (TF) is given by:

$$\frac{P(s)}{\Theta(s)} = \frac{V_m G_{PLL}(s)}{s + G_{PLL}(s) V_m}, \tag{2.4}$$

where $G_{PLL}$ is a PI controller, whose generic transfer function is:

$$G_{PLL}(s) = k_{p1} + \frac{k_{i1}}{s} = k_{p1}\frac{1+\tau_1 s}{\tau_1 s}, \tag{2.5}$$

where $k_{p1}$, $k_{i1}$ and $\tau_1 = k_{p1}/k_{i1}$ are the proportional, integral and constant time gain of the controller. Substituting (2.5) into equation (2.4) and comparing it with the rewritten TF in canonical form,

$$\frac{P(s)}{\Theta(s)} = \frac{2\xi w_{nt} s + w_{nt}^2}{s^2 + 2\xi w_{nt} s + w_{nt}^2}, \tag{2.6}$$

provides,

$$w_{nt} = \sqrt{\frac{k_{p1} V_m}{\tau_1}}, \tag{2.7}$$

$$\xi = \sqrt{\frac{V_m k_{p1} \tau}{2}}. \tag{2.8}$$

By Wiener method, define $\xi = 1/\sqrt{2}$ and $w_{nt} = w_n/3$ is a good compromise (CHUNG, 2000). Thus, the controller gains are described by:

$$k_{p1} = \frac{2 w_{nt} \xi}{V_m}, \tag{2.9}$$

$$k_{i1} = \frac{w_{nt}^2}{V_m}. \tag{2.10}$$

### 2.2.2 Active and Reactive Power Injection Control

The active power injection is controlled by the direct-axis ($d$) current $i_{gd}$ and the reactive power ($Q$) injection, by the quadrature-axis ($q$) current $i_{gq}$ in the internal loop, as shown in Fig. 5(b). This fact can be explained by the action of SRF-PLL, whose the $v_{gq}$ at the measurement point is zero. Therefore the expression of $Q$ injected to the grid is expressed by,

$$Q = -\frac{3}{2}(v_{gq} i_{gd} + v_{gd} i_{gq}) = -\frac{3}{2}(v_{gd} i_{gq}), \tag{2.11}$$

where $v_{gd}$ and $i_{gq}$ are the direct grid voltage and the quadrature grid current, respectively. Notably, without reactive compensation, the current $i_{gq}$ is zero.

The block diagram representing (2.11) is given in Fig. 7(a). The controller tuning of the inner loop takes into account the a.c side plant modeling. This approach can be found

in (ALMEIDA, 2011), in the $dq$ reference. Besides, the plants for the control of $i_{gd}$ and $i_{gq}$ are equal and, therefore, the controller gains of both inner loop are the same. Due to the current loop is sufficiently faster than the reactive power loop, it is possible to consider it ideal, i.e., $i_{gq} \cong i^*_{gq}$. Thus, Fig. 7(a) can be approximated to the Fig. 7(b) block diagram.

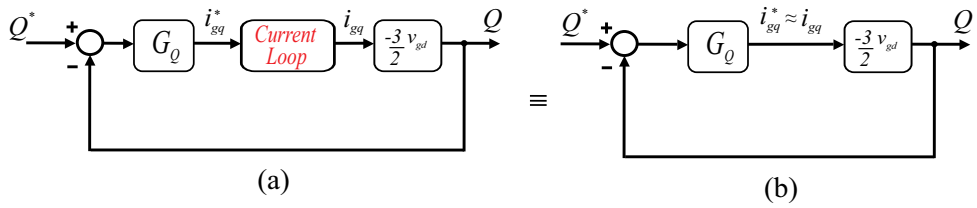


Figure 7 – (a) $Q$ control block diagram. (b) $Q$ control simplified block diagram.

The FT is given by:

$$\frac{Q(s)}{Q^*(s)} = \frac{\frac{-3v_{gd}}{2}G_Q(s)}{1 - \frac{3v_{gd}}{2}G_Q(s)}, \tag{2.12}$$

where $G_Q(s) = k_{p,Q} + k_{i,Q}/s$ is the PI controller. Defining $D = -3/2v_{gd}$ and rearranging (2.12), then:

$$\frac{Q(s)}{Q^*(s)} = \frac{1 + k_{p,Q}k_{i,Q}s}{1 + \frac{1+Dk_{p,Q}}{Dk_{i,Q}}s}, \tag{2.13}$$

Selecting the frequency $f_{z,Q}$ and $f_{p,Q}$ of the zero and pole, respectively, as 10 and 100 times lower than the inner loop pole frequency $f_i$:

$$f_{z,Q} = \frac{k_{i,Q}}{2\pi k_{p,Q}} = \frac{f_i}{10}, \tag{2.14}$$

$$f_{p,Q} = \frac{k_{i,Q}}{2\pi k_{p,Q}} = \frac{f_i}{100}. \tag{2.15}$$

The above approach ensures that the current loop will be 10 times faster than the $Q$ loop. Therefore, using the methodology of poles allocation, the PI controller gains are:

$$k_{p,Q} = \frac{2\pi f_{p,Q}}{2\pi D(f_{z,Q} - f_{p,Q})}, \tag{2.16}$$

$$k_{i,Q} = 2\pi f_{z,Q}k_{p,Q}. \tag{2.17}$$

The expression of the instantaneous active power $P$ in synchronous reference frame, considering the action of SRF-PLL, is:

$$P = \frac{3}{2}(v_{gd}i_{gd} + v_{gq}i_{gq}) = \frac{3}{2}(v_{gd}i_{gq}), \tag{2.18}$$

The PV inverter dc-side modeling indicates that the injected power is proportional to the $v_{dc}^2$ (XAVIER; CUPERTINO; PEREIRA, 2018). The PI controller calculates the reference $P^*$, which divided by $3/2v_d$ provides the reference $i_{gd}^*$ to the direct inner current loop.

All PI controllers were implemented in their discretized form. There are several discretization methods, such as Forward, Backward, Tustin and others. The Tustin method is used in this work, whose transformation from $s$ to $z$ is given by:

$$s = 2f_{sp}\frac{z-1}{z+1}, \tag{2.19}$$

where $f_{sp}$ is the sampling frequency.

### 2.2.3 Modulation Strategy

The pulse width modulation (PWM) is a widely used technique to determinate the switching signals of semiconductor devices due to the low-harmonic distortion waveform characteristics, fixed switching frequency and simple implementation (HAVA; KERKMAN; LIPO, 1999).

The most common strategies are sinusoidal modulation (SPWM) and space vector modulation (SVPWM). The SPWM consists of comparing a sinusoidal signal (to be synthesized by the PV inverter) with a triangular carrier at the switching frequency $f_{sw}$, generating the pulse sequence for the conduction of the IGBTs (gate signals). The SPWM modulator presents a linear region of operation, which is exploited in PV inverters. Thus, a limitation of the maximum voltage to be synthesized by the SPWM technique is closely related to the reference signal characteristic.

In three-phase applications, the neutral point is isolated and there is no neutral current path (HAVA; KERKMAN; LIPO, 1999). In these cases, the insertion of zero-sequence components becomes possible and allows greater utilization of the dc-link.

The SVPWM is based on the spatial phasors theory, which associates to each semiconductor device conduction state a spatial vector, in the complex plane. However, in this work, the SVPWM follows the methodology of (HAVA; KERKMAN; LIPO, 1999), by calculating the zero-sequence (third harmonic odd multiples) to be added into the sinusoidal signal to be synthesized by the inverter (reference). Fig. 8(a) shows the zero sequence signal calculator $v_0$, built by means of a smaller magnitude test.

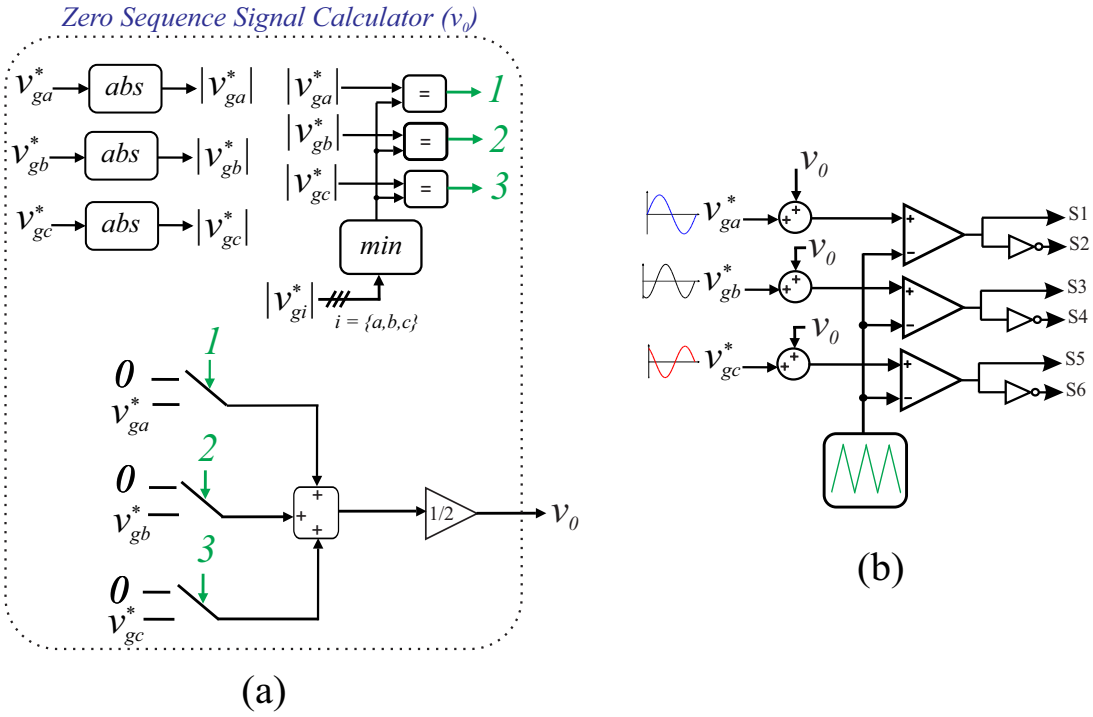


Figure 8 – (a) Zero sequence signal calculator ($v_0$) to be added into the reference. (b) Signal block diagram of the SVPWM employing the zero-sequence injection principle.

The reference signal with the smallest instantaneous absolute value among the three reference signals is chosen and is multiplied by 0.5, such as:

$$v_0 = \begin{cases} 0.5v^*_{ga}, if|v^*_{ga}| = min(|v^*_{ga}|, |v^*_{gb}|, |v^*_{gc}|) \\ 0.5v^*_{gb}, if|v^*_{gb}| = min(|v^*_{ga}|, |v^*_{gb}|, |v^*_{gc}|) \\ 0.5v^*_{gc}, if|v^*_{gc}| = min(|v^*_{ga}|, |v^*_{gb}|, |v^*_{gc}|). \end{cases} \tag{2.20}$$

Finally, this zero-sequence component is added to the phase references. Fig. 9(a) shows the input comparator signal after the addition of the zero-sequence component, as well as the respective gate signals, in Fig. 9(b).

Fig. 9(c) shows a zoom of the zero-sequence signal, the phase reference signal ($v^*_{ga}$) and the sum of $v_0$ and $v^*_{ga}$. Besides, the spectrum analysis of $v_0$ shows zero-sequence components, i.e., third harmonic odd multiples.

## 2.3 Physics-of-Failure of IGBT Modules

The power modules reliability is defined as the ability to perform their function under rated conditions for a certain period of time (WANG et al., 2014). Currently, several efforts in the literature are focused in the reliability of power systems, i.e. PV inverters connected to the grid.

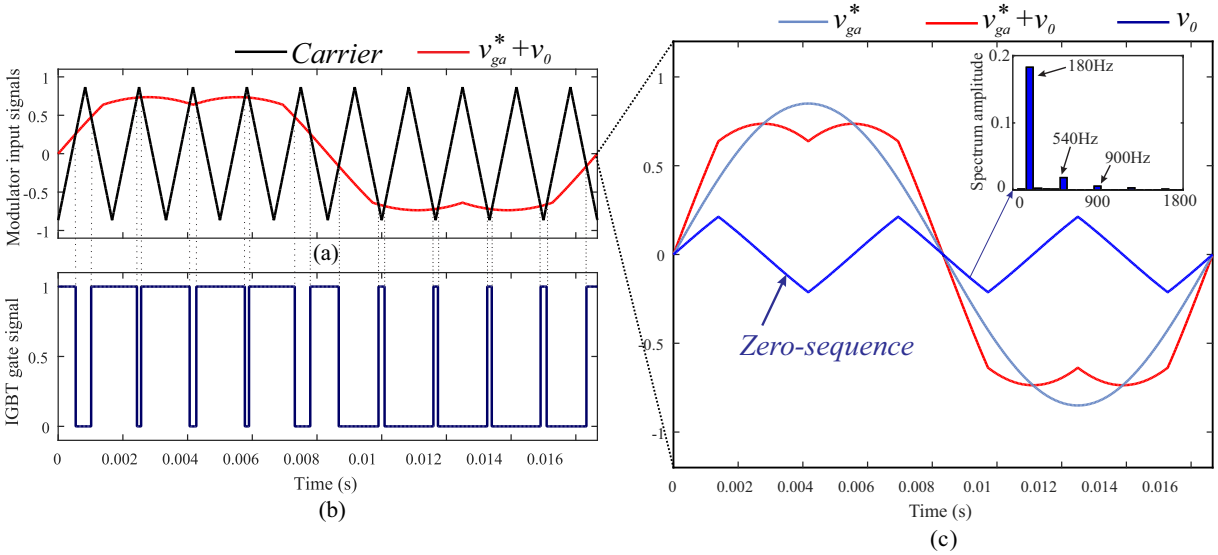


Figure 9 – (a) Typical input waveforms of the SVPWM modulator. (b) IGBT gate signals. (c) Zoom of the $v_0$, $v_{ga}^*$ and the sum of $v_0$ and $v_{ga}^*$.

There are several PV inverter components that can cause system failure. The d.c-link electrolytic capacitors and the power modules (IGBTs and anti-parallel diodes) are the main sources of failure in the PV inverter. A complete analysis of all these components would be very complex, since they may have a cross-effect of the reliability on each other (YANG; SANGWONGWANICH; BLAABJERG, 2016). In order to simplify the reliability analysis, only the temperature-related failure mechanisms of the IGBT are considered in this work.

Understanding the physical of failure (PoF) mechanisms in power modules is essential to infer in the devices reliability. The PoF approach is based on the analysis of each device failure mechanism. There are two predominant failure mechanisms: wear-out and catastrophic failures, as shown in the flowchart of Fig. 10.

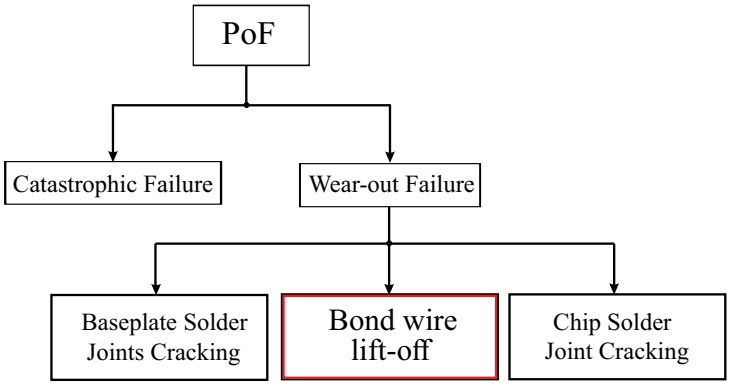


Figure 10 – Flowchart of IGBT physics failure types.

Catastrophic failures occur caused by single event overstress, such as short-circuits (WANG et al., 2014). Besides, it is difficult to predict and often lead to serious consequences

for PV inverter, for example.

Unlikely catastrophic failures, wear-out failures are more predictable, since the IGBT operating conditions are known. There are three main wear-out failure mechanisms on the IGBT modules due to thermal stress: the bond wire lift-off, solder joints cracking under the chip and solder joints cracking under the baseplate (WANG et al., 2014; CHUNG, 2000).

Among the three mechanisms of wear-out failure, this study focuses on bond wire lift-off, whose failure is usually due to three factors (REIGOSA et al., 2016):

1. Heel fractures: an irreversible deformation is induced by the temperature swings and the material enters into the plastic region, leading to stress formation in the packaging and continuous degradation;
2. Wire bond lift-off: As the wire is made of aluminum (Al) and the power devices are made of silicon (Si), mechanical stresses are induced at the Al-Si interface due to the different thermal expansion coefficient of these two materials;
3. Metallurgical damage: caused by thermal stresses during the manufacturing process.

## 2.4 Lifetime Models

(REIGOSA et al., 2016) reviews the lifetime prediction study of semiconductor devices and divides them into three categories:

1. Lifetime prediction based on constant failure rate models, from various handbooks (MIL-HDBK-217E, 1991);
2. Lifetime prediction based on empirical lifetime models developed by means of accelerated tests (HELD et al., 1997; NORRIS; LANDZBERG, 1969; BAYERER et al., 2008);
3. Lifetime prediction based in the physical failure mechanisms.

The first category is no longer used due to its limitations and the improvement of the other two. The second one is the most widely used method for the lifetime prediction of IGBT modules, while the third one is limited due to the lack of detailed information of the IGBT modules materials.

Several empirical lifetime models of the IGBT module (2nd category) can be found in the literature.

### 2.4.1 Coffin-Manson Model

It was proposed by (MANSON, 1966) and is the simplest lifetime model:

$$N_f = A(\Delta T_j)^{-n}, \tag{2.21}$$

where $N_f$ is the number of cycles to failure; $A$ and $n$ are empirical constants. This model only considers the junction temperature fluctuation $\Delta T_j$ as input parameter, not taking into account the frequency of cycles which may lead to inaccuracies.

### 2.4.2 Coffin-Manson-Arrhenius Model

The description of the lifetime model can be found in (HELD et al., 1997). This model additionally considers the effect of the average junction temperature $T_{jm}$ when compared to the previous model. Thus,

$$N_f = A(\Delta T_j)^{-n} exp\left(\frac{E_a}{k_b T_{jm}}\right), \tag{2.22}$$

where $k_b$ is the Boltzmann constant and $E_a$ being the activation energy.

### 2.4.3 Coffin-Manson-Arrhenius-Landzberg Model

(NORRIS; LANDZBERG, 1969) verified that the lifetime model would best fit considering the inclusion of frequency of thermal cycling $f$. Therefore, the collection of contributions from previous models provides the following model:

$$N_f = A f^{\alpha} (\Delta T_j)^{-n} exp\left(\frac{E_a}{k_b T_{jm}}\right), \tag{2.23}$$

where $\alpha$ is an empirical constant.

### 2.4.4 Bayerer Model

The Bayerer's model is the most complete lifetime model (FERREIRA et al., 2017) explained until here and can be found in (BAYERER et al., 2008). This model includes the cycle heating time $t_{on}$ effect together with the impact of other bond wire parameters:

$$N_f = A \Delta T_j^{\beta_1} exp\left(\frac{\beta_2}{T_{jm} + 273}\right) t_{on}^{\beta_3} I^{\beta_4} V^{\beta_5} D^{\beta_6}, \tag{2.24}$$

where $A$ and $\beta$ coefficients are obtained via accelerated thermal tests. $I$ is the current per bond foot, $V$ is the blocking voltage and $D$ is the bond wire diameter.

## 2.5 Reactive Power as Ancillary Service of the Multifunctional PV Inverter

Basically there are three important reasons for reactive power injection as ancillary service by PV inverter, listed below:

1. During operation under low solar irradiance, the PV inverter has a current margin to provide reactive power to the load, reducing the $Q$ consumption from the grid, reducing transmission losses and improving the system stability and power quality.
2. The $Q$ injection control allows voltage regulation at the point of common coupling (PCC) of the PV inverter with the grid;
3. In transient disturbances, such as overvoltages or voltage sags, the $Q$ injection control assists the recovery of the PCC voltage.

Due to the above advantages, many countries are updating their grid codes, such as Japan, Germany, Italy, Spain and others (XAVIER; CUPERTINO; PEREIRA, 2018). Before, the inverter should immediately disconnect from the grid during a fault. With the new updates, the grid code allows the PV inverter to inject reactive current to support voltage recovery during a grid fault.

# 3 Methodology

In this chapter, the methodology used to evaluate the lifetime of semiconductor devices will be presented. In addition, a power losses analysis in power modules using mathematical models will be provided to justify some results in the next chapter.

## 3.1 Power Losses Analysis in Electronics Devices with Reactive Power Injection

Under perfectly balanced conditions and disregarding the effect of the switching harmonics, the apparent power $S$ injected into the grid increases according to the compensated reactive power, as demonstrated by:

$$S = \sqrt{P^2 + Q^2} = \sqrt{3} V_g I_g. \tag{3.1}$$

where $I_g$ and $V_g$ are the $rms$ values of the grid current and voltage, respectively. Considering the grid as an infinite bus, then the increased $S$ implies in increased injected current $I_g$. These results are presented in Fig. 11 for the two cases: with 8kVAr and zero $Q$ injection.

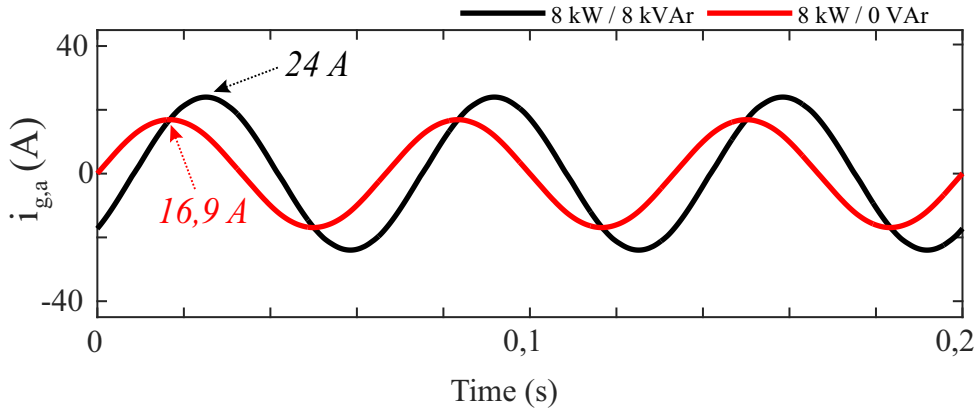


Figure 11 – Phase current injected into the grid with and without reactive power injection.

The amplitude of the current increases by 41.42% when 8 kVAr is injected into the grid. In addition, the currents with and without $Q$ compensation are not in phase, reducing the PF. The operation under non unitary PF condition can directly impact the thermal loading in the inverter semiconductor devices, e.g., diode and IGBT. Thus, the relationship between apparent power injection and power losses will be evaluated analytically at first.

The total power losses ($P_{tot}$) on power module is described as a sum of switching and conduction losses, as follows:

$$P_{tot} = P_c + P_{sw}, \tag{3.2}$$

where $P_c$ and $P_{sw}$ refer to the sum of IGBT and diode conduction and switching losses, respectively. The IGBT and diode conduction losses are modeled considering that the current and voltage waveforms are displaced by an angle $\theta$. The current and voltage of the phase $a$ at the inverter output are defined by:

$$i_{ga} = I_{cm} sin(\alpha), \tag{3.3}$$

$$v_{ga} = V_{cm} sin(\alpha + \theta), \tag{3.4}$$

where $\alpha = 377t$, $I_{cm}$ and $V_{cm}$ are the current and voltage phase amplitude, respectively. As shown in Fig. 12(b), the typical collector-emitter voltage $v_{ce}$ and collector current $i_c$ of the IGBT can be approximated by a linear equation in its operating range, as well as the forward voltage $v_f$ and forward current $i_f$ of the diode in Fig. 12(a) (CASANELLAS, 1994):

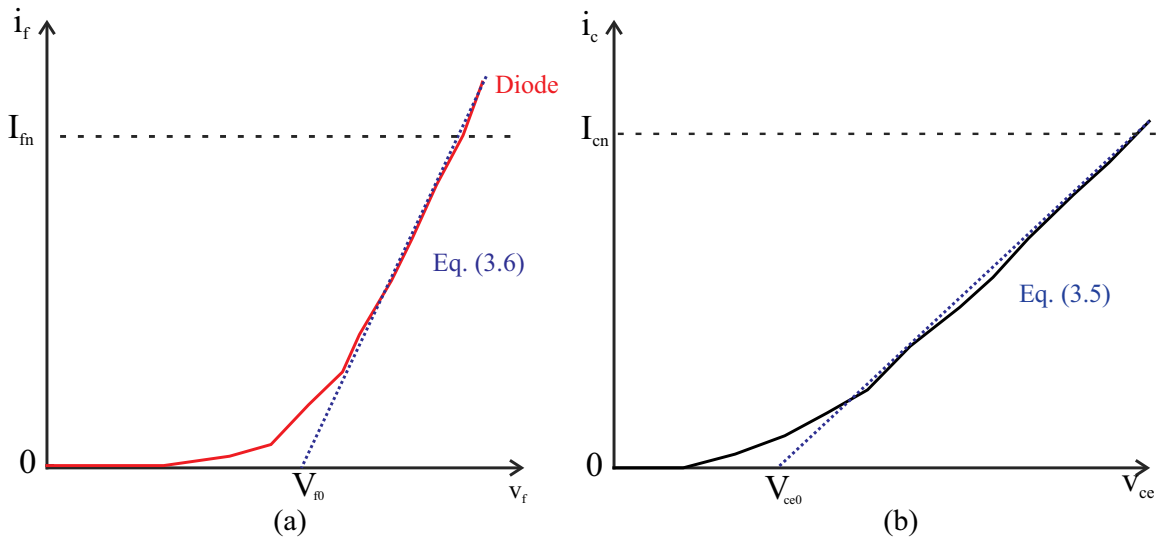


Figure 12 – The characteristic curves: (a) $v_f$ x $i_f$ of the diode, (b) $v_{ce}$ x $i_c$ of the IGBT and the linear approximation for both.

$$v_{ce} = \left(\frac{V_{cen} - V_{ce0}}{I_{cn}}\right) i_c + V_{ce0} = r_i i_c + V_{ce0}, \tag{3.5}$$

$$v_f = \left(\frac{V_{fn} - V_{f0}}{I_{cn}}\right) i_c + V_{f0} = r_{di} i_c + V_{f0}, \tag{3.6}$$

where $V_{cen}$, $V_{ce0}$, $V_{fn}$, $V_{f0}$, $I_{cn}$, $r_i$ and $r_{di}$ are collector-emitter voltage for rated operating condition, IGBT on-state zero current collector-emitter voltage, forward diode voltage for rated condition, on-state zero current voltage across the diode, rated collector current, collector-emitter on-state resistance and diode on-state resistance, respectively. All these parameters are easily found on component manufacturers' datasheets.

In (BIERHOFF; FUCHS, 2004), the authors show that the conduction losses for SVPWM may be computed in the same way as a sine-triangular PWM (SPWM), representing a good approximation. However, for a more accurate approach, it is considered the insertion of zero sequence components (odd harmonics multiples of 3) in the sine modulation function $h(\alpha + \theta)$ (CASANELLAS, 1994), as follows:

$$h(\alpha + \theta) = sin(\alpha + \theta) + \frac{1}{6} sin\left[3(\alpha + \theta)\right]. \tag{3.7}$$

It is important to note that the zero-sequence component of (3.7) is not the same as that applied to the SVPWM modulator described in the previous chapter, but it is an approximation to facilitate the modeling. Furthermore, the duty cycle $\delta$ of the voltage pulses is obtained by comparing the modulation signal $h(\alpha + \theta)$ with the carrier signal, given by:

$$\delta = \frac{1}{2}\left[1 + mh(\alpha + \theta)\right], \tag{3.8}$$

where $m = \sqrt{3}V_{cm}/v_{dc}$ is the modulation index. Fig. 13 shows the current $i_c$ flowing through the IGBT S1. It is possible to express the $i_c$ as the product of the inverter output phase current $i_a$ and the duty cycle (3.8), as follows:

$$i_c = i_a\delta = I_{cm} sen(\alpha)\delta. \tag{3.9}$$

From $\alpha = 0$ to $\alpha = \pi$, S1 conducts for a time $\delta T_s$, where $T_s$ is the switching period. After this time, $i_a$ is still positive and current has to flow through the lower diode in phase $a$, D2, for $(1 - \delta)T_s$.

### 3.1.1 Analytical Mathematical Model of Conduction Power Losses

The IGBT conduction losses $P_{c,I}$ are calculated by (BIERHOFF; FUCHS, 2004):

$$P_{c,I} = \frac{1}{2\pi}\int_0^{\pi} v_{ce} i_c \delta d\alpha. \tag{3.10}$$

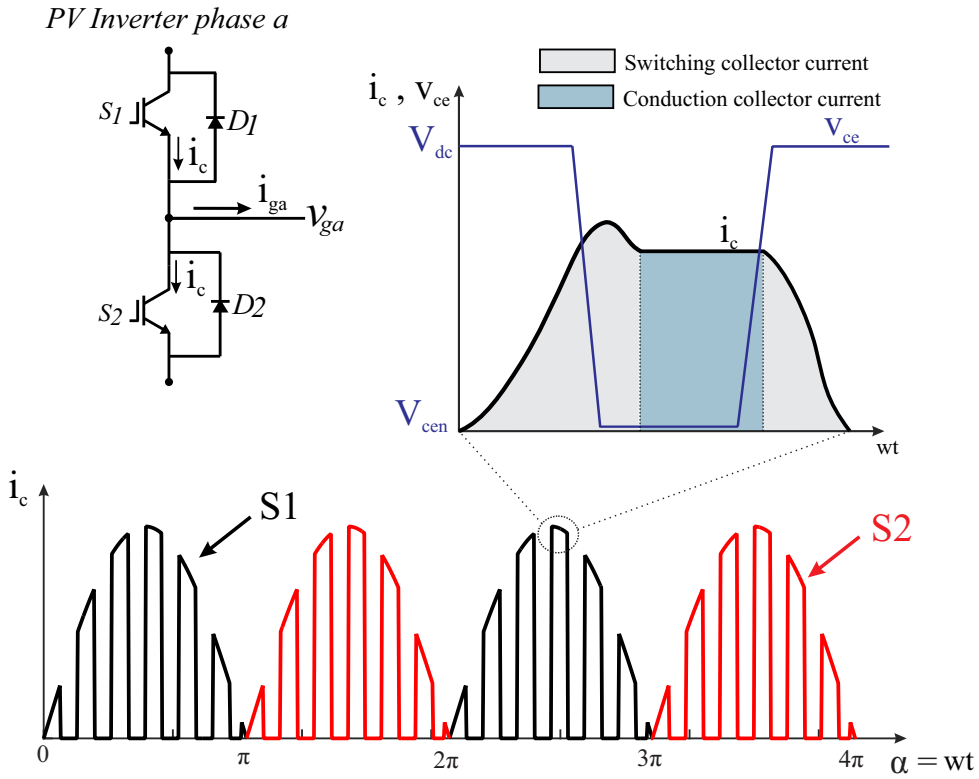


Figure 13 – Collector currents $i_c$ of IGBTs S1 and S2. Zoom in the typical waveforms of switching and conduction current of IGBT S1.

Similarly, the diode conduction losses $P_{c,D}$ are given by:

$$P_{c,D} = \frac{1}{2\pi}\int_0^{\pi} v_{ce} i_c (1-\delta) d\alpha. \tag{3.11}$$

Substituting (3.5), (3.6), (3.9) and (3.8) and resolving (3.10) and (3.11) applying several math manipulations, the conduction losses obtained for IGBT and diode are given by (3.12) and (3.13), respectively:

$$P_{c,I} = \left[\frac{1}{8} + \frac{m}{3\pi}cos(\theta) - \frac{m}{30\pi}cos(3\theta)\right] I_{cm}^2 r_i + \left[\frac{1}{2\pi} + \frac{m}{8}cos(\theta)\right] V_{ce0} I_{cm}, \tag{3.12}$$

$$P_{c,D} = \left[\frac{1}{8} - \frac{m}{3\pi}cos(\theta) + \frac{m}{30\pi}cos(3\theta)\right] I_{cm}^2 r_{di} + \left[\frac{1}{2\pi} - \frac{m}{8}cos(\theta)\right] V_{f0} I_{cm}. \tag{3.13}$$

### 3.1.2 Analytical Mathematical Model of Switching Power Losses

In contrast to the conduction losses, the switching losses do not directly depend on the modulation function (BIERHOFF; FUCHS, 2004). The energy required to switch the IGBT is presented as graphs in the datasheets provided by the device manufacturer.

Reference (CASANELLAS, 1994) analyzes a typical switching curve of an IGBT, approaching some parameters to simplify the calculations. The average switching power losses ($P_{on,I}$ and $P_{off,I}$), considering the angle $\theta$ between the voltage and the current, follow the methodology applied in (CASANELLAS, 1994) and are given by (3.14) and (3.15). More details can be found in Appendix A.

$$P_{on,I} = \frac{f_{sw} v_{dc}}{2\pi}\left[\frac{\pi I_{cm}^2 t_{rn}}{4 I_{cn}} + 2Q_{rrn}\left(0.28\pi + 0.38\frac{I_{cm}}{I_{cn}} + 0.015\pi\frac{I_{cm}^2}{I_{cn}^2}\right) + \left(1.6 I_{cm} + 0.1\pi\frac{I_{cm}^2}{I_{cn}}\right) t_{rrn}\right]. \tag{3.14}$$

$$P_{off,I} = \frac{f_{sw} v_{dc} I_{cm} t_{fn}}{2\pi}\left(\frac{2}{3} + \frac{\pi I_{cm}}{12 I_{cn}}\right), \tag{3.15}$$

where $I_{cn}$ gives the IGBT rated collector current, $t_{rn}$ is the rated IGBT current rise time, $Q_{rrn}$ is nominal reverse diode recovery load, $t_{rrn}$ is the diode nominal reverse recovery time and $t_{fn}$ is the rated IGBT current fall time. Finally, the IGBT total switching losses is the sum of $P_{on,I}$ and $P_{off,I}$.

The turn-on switching energy of diodes is usually negligible (ANURAG; YANG; BLAABJERG, 2015b), while the turn-off switching losses ($P_{off,D}$) can be approximated by (CASANELLAS, 1994):

$$P_{off,D} = \frac{f_{sw} v_{dc} Q_{rrn}}{2\pi}\left[0.28\pi + 0.38\frac{I_{cm}}{I_{cn}}\right]. \tag{3.16}$$

Equations (3.12)-(3.13) and (3.14)-(3.16) demonstrate that the conduction power losses strongly depend on $\theta$, while the switching power losses are not influenced by $\theta$. Tab. 1 presents the typical values used to obtain the power losses curves in Fig. 14.

Table 1 – Typical values of the parameters from power losses equations found in the IGBTs and diodes datasheets.

| Parameter | Label | Value |
|---|---|---|
| IGBT collector-emitter voltage for rated operation | $V_{cen}$ | 2V |
| IGBT on-state zero current collector-emitter voltage | $V_{ceo}$ | 0.8 V |
| IGBT rated collector current | $I_{cn}$ | 25 A |
| Forward diode voltage for rated condition | $V_{fn}$ | 1.7 V |
| On-state zero current voltage across the diode | $V_{fo}$ | 0.5 V |
| Rated IGBT current rise time | $t_{rn}$ | 30 ns |
| Rated IGBT current fall time | $t_{fn}$ | 70 ns |
| Diode nominal reverse recovery time | $t_{rrn}$ | 200ns |
| Nominal reverse diode recovery load | $Q_{rrn}$ | 2.3 $\mu$C |

Fig. 14(a) shows the conduction losses for variations of $\theta$ when the converter injects fixed 8kVA with different modulation indexes (0.70 to 1). With $S$ constant, the current

amplitude injected in the grid is also constant. In the subsequent analyzes, the amplitude of the current and the apparent power injected are no longer kept constant.

When $0 < |\theta| < \pi/2$, the converter operates as an inverter and if $\pi/2 < |\theta| < \pi$, the converter operates as a rectifier. Fig. 14 (b) shows the switching power losses with $\theta$ variation.

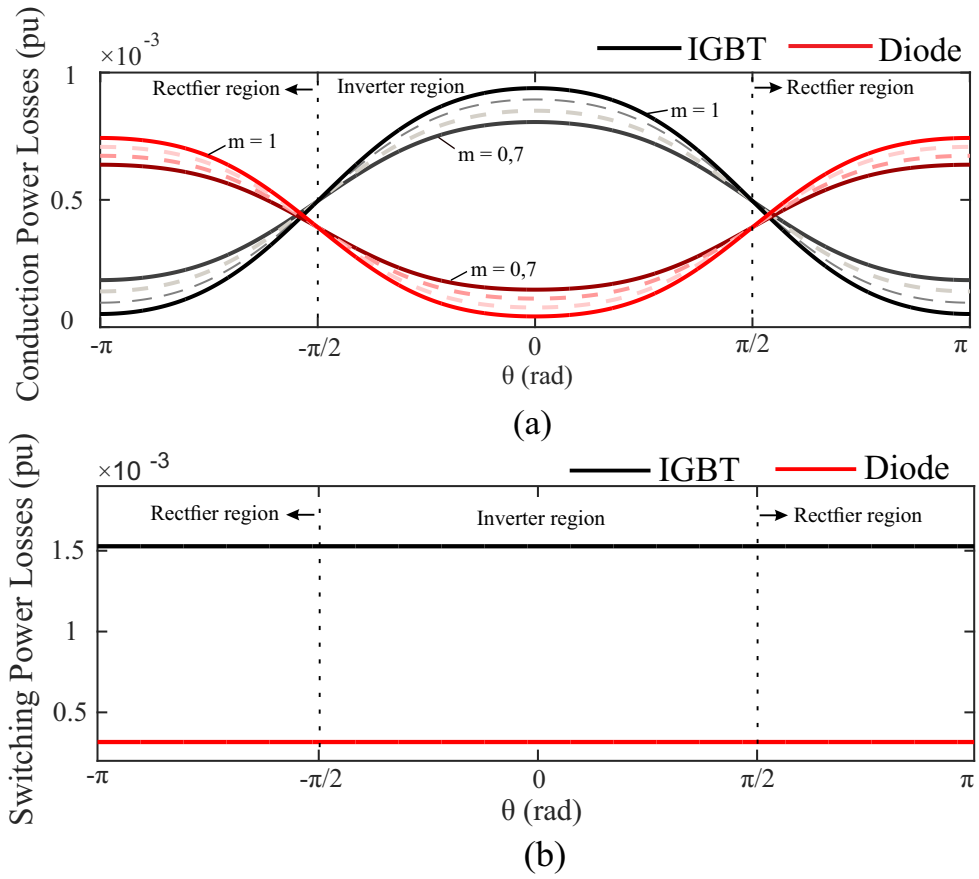


Figure 14 – Analysis of (a) conduction power losses, and (b) switching power losses, for variations of $\theta$ from $-\pi$ to $\pi$ and $S_{base} = 8$ kVA.

Regarding the power devices, the IGBT presents higher power losses than the diode during the inverter operation mode. In addition, the maximum conduction power losses occur when $\theta = 0$, i.e., PF is unitary. On the other hand, the diode conduction losses increase considerably when the reactive power injection increases. Furthermore, the greatest stress of the diode occurs in the rectifier region, which is not explored in PV inverters. The IGBT conduction power losses tend to reduce when the inverter operates under PF $< 1$, regardless of whether the FP is inductive or capacitive. This fact can be explained due to the presence of cosines (even function) in these equations, since $cos(\theta) = cos(-\theta)$.

Another interesting fact is the low sensitivity of the diode reverse recovery losses and the IGBT switching power losses with the operating PF variation. Although the proposed model does not show variations of the switching power losses with the PF, it should be clear that small variations in these power losses are noticed for an experimental

study, since there are voltage fluctuations in the dc-link, distortions in the current injected in the utility grid, dead time, minimum pulse filter and others, which were not considered in obtaining the above equations.

Despite some peculiarities observed in the switching losses, the $Q$ injection affects the dynamics of semiconductor devices. A case study is performed in the next sections to evaluate the reliability of power modules and the entire system (group of six modules) for this case.

## 3.2 Thermal Modeling of PV Inverter

There are two packaging methods for IGBT: press-pack packaging and module packaging. For historical reasons, the second method is the widely used due to its lower cost, simpler maintenance and mounting. However, the power module has large thermal resistance due to soldering and bond wire of internal chips. As a consequence, greater thermal stress in the module layers is observed, which impacts its failure rate (XIONG et al., 2008; REIGOSA, 2014).

The structure of a common IGBT module is composed of several layers of different materials, as shown in Fig. 15. $Z_{th_{(jc)}}$ refers to the transient thermal impedance between the junction of the IGBT chips and the case module, $Z_{th_{(ch)}}$ refers to the thermal impedance between case module and heatsink and $Z_{th_{(ha)}}$ is the transient thermal impedance between heatsink and ambient.

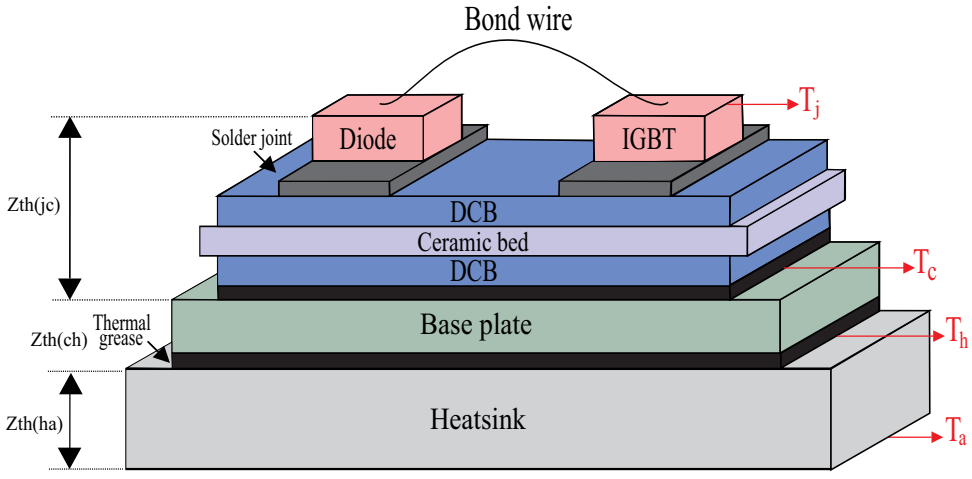


Figure 15 – Structure of a standard IGBT module.

As seen in the previous chapter, there are are three main wear-out failure mechanisms on the IGBT modules due to cyclic thermal stress: the bond wire lift-off, solder joints cracking under the chip (diode and IGBT) and solder joints cracking under the direct copper-bonded (DCB). In this work, the bond-wire failures are treated due to

thermal cycling. Thus, it is necessary to estimate the junction temperature $T_j$ of the device obtained from the considered mission profile.

### 3.2.1 Thermal Equivalent Circuit Models

The thermal behavior of the semiconductor components can be described by several circuit models, as the Foster and Cauer models.

The Cauer model reflects in the actual physical configuration of the semiconductor based on capacitances with intermediate thermal resistances, as observed in Fig. 16(a). The circuit nodes allow access to the internal temperatures of each layer of the semiconductor device.

The Foster model does not have any physical representation, been a fitting of the temperature transient curve provided by the manufacturers. This configuration is used in datasheets and is shown in Fig. 16(b).

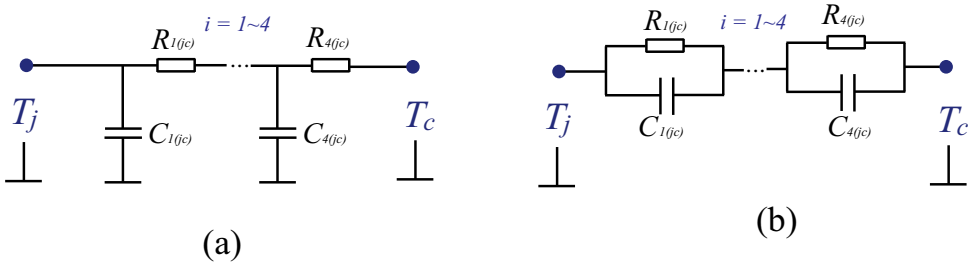


Figure 16 – Thermal (a) Cauer-model. (b) Foster-model.

$R_{i(jc)}$ represents the thermal resistance of the device layers and $C_{i(jc)}$ represents the thermal capacitance. The first one determines the steady-state mean value of the junction temperature and the second dictates the dynamic change or fluctuation of the junction temperature, by means of the time constant $\tau$, defined by:

$$\tau_i = R_{i(jc)} C_{i(jc)}. \tag{3.17}$$

Regarding the PV inverter design, a 1200V/25A IGBT, with part number IKW25T120 from Infineon, was selected once the three-phase PV inverter under analysis is rated at 12.15 $A_{rms}$. In addition, the 0.5 K/W heatsink is designed to achieve an average junction temperature of 100 °C at the rated conditions of the PV inverter without reactive power compensation, for safety operation reasons. The thermal parameters, found in datasheet, are presented in Tab. 2.

Table 2 – Foster thermal impedance for IKW25T120 power module from Infineon.

| Thermal impedance | | $Z_{th(jc)}$ | | | | $Z_{th(ch)}$ |
|---|---|---|---|---|---|---|
| | | 1 | 2 | 3 | 4 | |
| IGBT | R (K/W) | 0.229 | 0.192 | 0.174 | 0.055 | 0.65 |
| | $\tau$ (s) | 0.11 | 0.0156 | 0.00135 | 0.000152 | 0 |
| Diode | R (K/W) | 0.282 | 0.317 | 0.294 | 0.107 | 1 |
| | $\tau$ (s) | 0.101 | 0.0115 | 0.0013 | 0.000153 | 0 |

## 3.3 Lifetime Evaluation Procedure

The mission profile of solar irradiance ($G$) and ambient temperature ($T_a$) are obtained from Aalborg, Denmark. Besides, the reactive power profile is obtained from a real food industry. These profiles are sampled at one second with one year duration, as shown in Fig. 17.

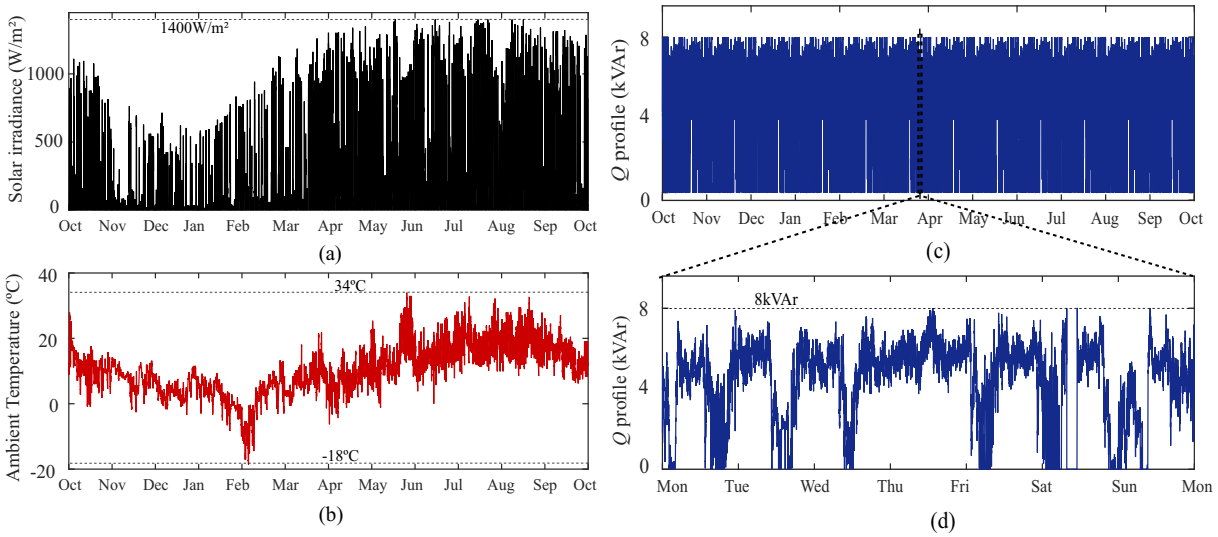


Figure 17 – Mission profile of: (a) Solar irradiance 1-year profile. (b) Ambient temperature 1-year profile. (c) Reactive power injection 1-year profile, according to the load requirement. (d) Zoom of reactive power injection 1-week profile.

Knowledge about the PV inverter operating conditions is essential in the lifetime study (SANGWONGWANICH et al., 2018; YANG; SANGWONGWANICH; BLAABJERG, 2016; MA et al., 2015; MA; BLAABJERG, 2012). During reactive power compensation, the inverter may be operating under higher thermal stress conditions. Therefore, the mission profile has a strong impact on the PV system reliability. In order to obtain the junction temperature $T_j$ of the power modules, the mission profile must be translated into a thermal loading (YANG; SANGWONGWANICH; BLAABJERG, 2016).

The Fig. 18 shows the main steps to translate the profiles into thermal loading. The active power $P_{in}$ is obtained from the PV system model considering the mission profile as

input (VILLALVA; GAZOLI; FILHO, 2009).

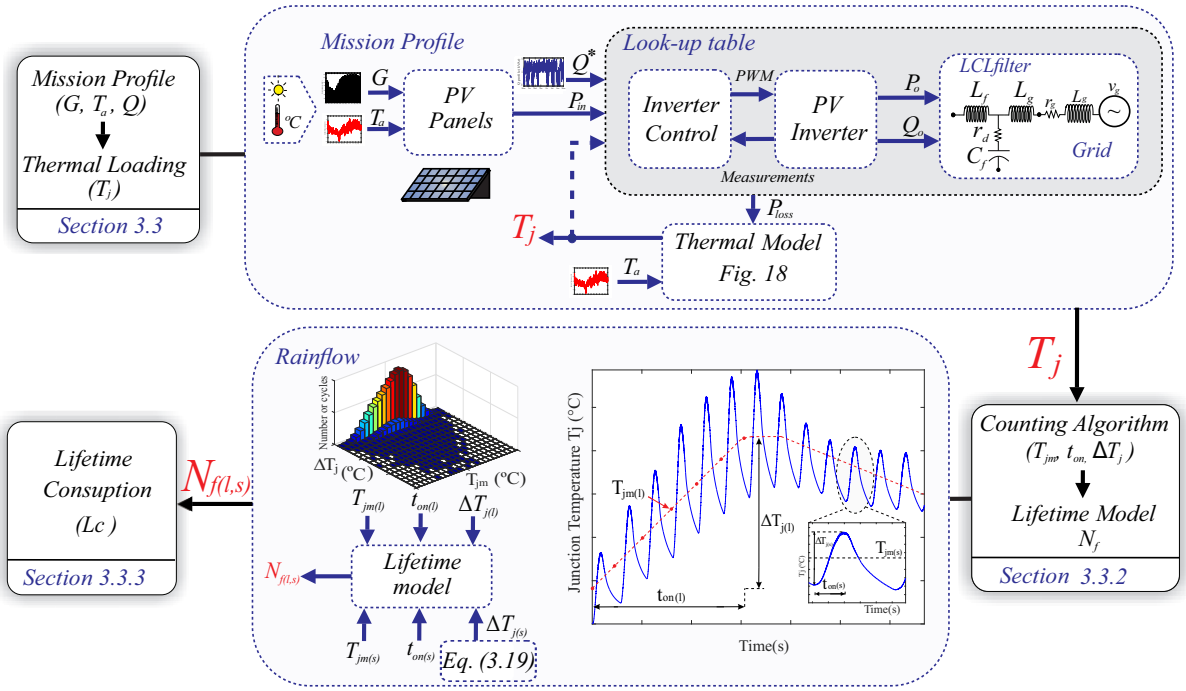


Figure 18 – Flowchart for the lifetime evaluation of power devices.

The calculation of the total power losses is implemented with a look-up table, obtained from a certain set of operating conditions: reactive and active power injection as well as fixed junction temperature. This procedure is performed at $PLECs$ simulation environment. Therefore, the power losses under other conditions given by the mission profiles can be interpolated from the look-up table.

### 3.3.1 Electro-Thermal Hybrid Model

The thermal model of power semiconductors devices can be modeled as series thermal resistance $R$ and capacitance $C$ networks (MA, 2015). The total power losses $P_{tot}$ flow through the semiconductor junction to the power device case. In the sequence, the power losses flow through the case to the heatsink, where there is heat exchanged by convection with the environment.

According to (ANDRESEN et al., 2015), the thermal Foster and Cauer-model described previously have their limitations to correctly estimate the case and junction temperature of power semiconductor devices. Thus, in (MA, 2015) is proposed a new thermal model which combines the advantages of these two thermal models, as shown in Fig. 19.

The thermal model presents two paths. The lower path is used to estimate the junction temperature, by means of the multilayer Foster network based on the semiconductor devices datasheets. The case temperature in this path is determined by the $T_c$ of

the upper path. This ensures that the Foster network is correctly used, avoiding abrupt case temperature changes.

The upper path is responsible for estimating the case and heatsink temperature and not the junction temperature. The multilayer Foster network is mathematically transformed into a single-layer equivalent Cauer network. As a result, this electro-thermal model estimates the case temperature $T_c$ in the upper path and feed it into the Foster equivalent circuit, in order to obtain a better estimate of $T_j$ (MA et al., 2015). Thus, with the values of the devices total power losses estimated from the mission profile conditions, it is possible to obtain the junction temperature profile with the model of Fig. 19.

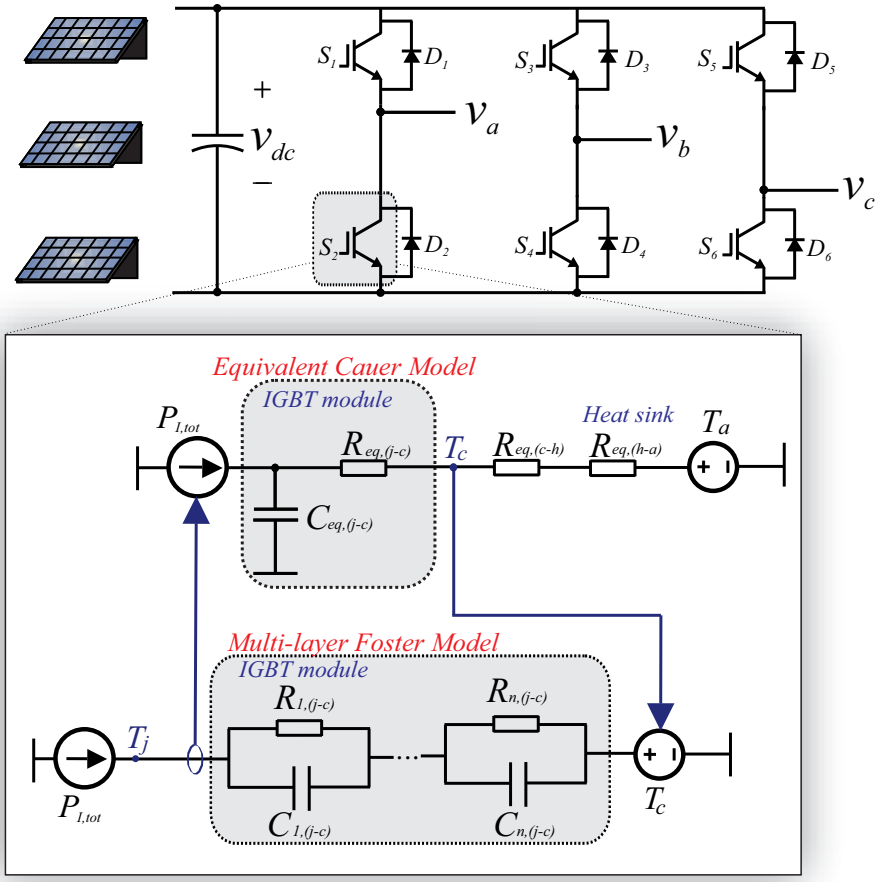


Figure 19 – Thermal model to estimate junction temperature. Adapted from (MA et al., 2015).

### 3.3.2 Lifetime Evaluation for Different Time Constants

The use of lifetime models requires three factors that directly affect the degradation of semiconductor devices, such as: heating time during the cycling period $t_{on}$, mean junction temperature $T_{jm}$ and cycle amplitude $\Delta T_j$. It is important to note that the thermal stresses

in the power devices present different behaviors, according to two time constants (MA et al., 2015):

1. Thermal cycling due to climatic variations (referred to as long-term); and
2. Thermal cycling due to grid frequency (referred to as short-term).

Fig. 20 shows that the long-term time constant (with index $l$) does not have well-defined thermal cycles. This is explained by an irregular mission profile dynamics (SANGWONGWANICH et al., 2018; YANG; SANGWONGWANICH; BLAABJERG, 2016; MA et al., 2015; MA; BLAABJERG, 2012). Thus, a counting algorithm (e.g. rainflow algorithm) is employed in order to find regular thermal loading cycles. It allows obtaining $t_{on(l)}$, $\Delta T_{j(l)}$ and $T_{jm(l)}$, which are applied to the lifetime model (GOPIREDDY et al., 2015).

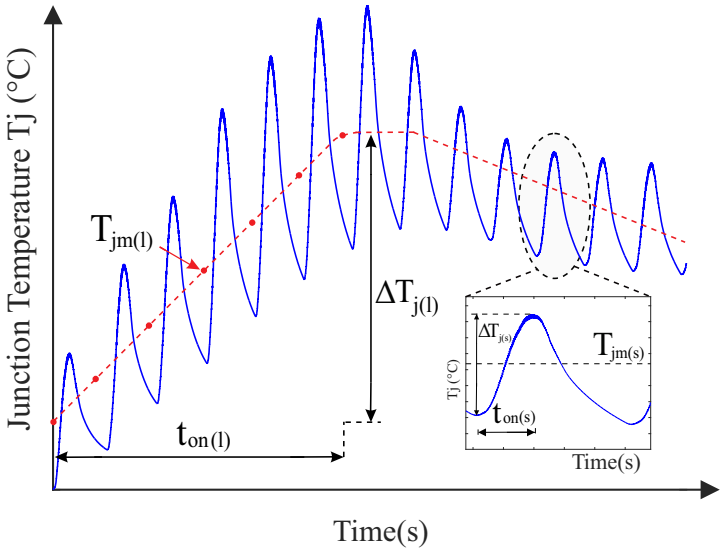


Figure 20 – Thermal cycling due to the grid frequency (index $s$) and due to climatic variations (index $l$).

The short-term time constant (represented with index $s$) has well-defined thermal cycles caused by the grid frequency oscillations. Thus, $t_{on(s)} = 1/(2f_n)$ (MA et al., 2015). Therefore, it is not necessary to use thermal cycling counting algorithms in this case (MA et al., 2015). The junction temperature $T_j$ obtained from the equivalent thermal model is the average junction temperature $T_{jm(s)}$ and can be directly applied to the lifetime model. In order to calculate $\Delta T_{j(s)}$, it is necessary to find the maximum and minimum values of the $T_j$ thermal cycles. However, this is not an easy task, since deriving the equation that describes the junction temperature (deducted by (MA; BLAABJERG, 2012)) to find the maximum and minimum of $T_j$ is not simple.

It is known that the current flowing through the IGBT is pulsed, i.e, the IGBT is activated by a half-cycle, while the diode is activated by the complementary time. In the

same way, the IGBT power losses have the same shape as the current, as shown in Fig. 21(a). Therefore, a simplification to determine $\Delta T_{j(s)}$ is proposed by (MA; BLAABJERG, 2012). The methodology consists of approximating the waveform of the IGBT power losses by a known waveform defined by a sum of pulses, with the same original $P_{I,tot}$ area. In this case, the time when $T_j$ is maximum can be determined, in order to calculate $\Delta T_{j(s)}$.

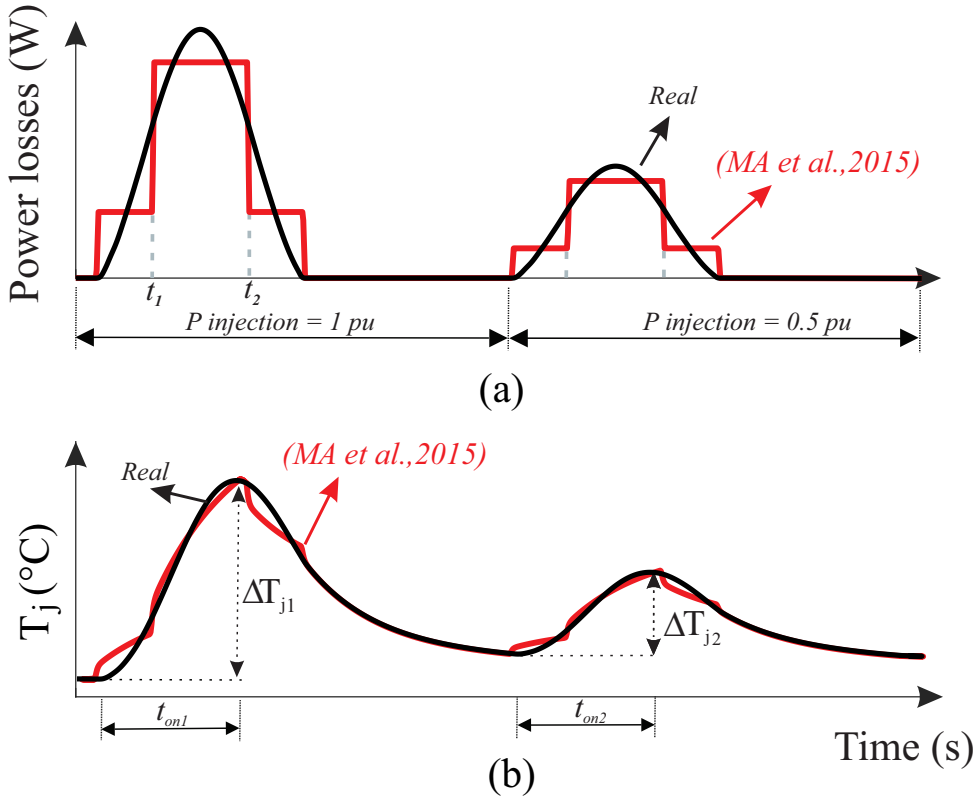


Figure 21 – (a) Real pulsed power losses and two steps power losses pulses approximation. (b) Junction temperature corresponding to the two-pulses approximation and real junction temperature.

The time-based expression of device thermal impedance $Z_{th}$ is expressed as (INFINEON, 2015):

$$Z_{th}(t) = \sum_{i=1}^{4} R_i \left[1 - exp\left(\frac{-t}{\tau_i}\right)\right] \tag{3.18}$$

where $R$ is the thermal resistance, which can be found in the component datasheet, and $\tau$ is calculated by (3.17). The time expression of the junction temperature variation is given by the product of the thermal impedance and the power losses of the semiconductor device. Once the steps times are set at $t_1 = 1/(8f_n)$ and $t_2 = 3/(8f_n)$, the cycling amplitude caused by the grid frequency of the junction temperature can be analytically determined

by (MA et al., 2015; MA; BLAABJERG, 2012):

$$\Delta T_{j(s)} = P_{I,tot} Z_{th}\left(t_2 = \frac{3}{8 f_n}\right) + 2 P_{I,tot} Z_{th}\left(t_2 - t_1 = \frac{1}{4 f_n}\right), \tag{3.19}$$

The Fig. 21(b) shows the respective approximate and real junction temperatures, calculated according to the waveforms shown in Fig. 21(a). The approximate $T_j$ calculation methodology shows an acceptable consistency of junction temperature fluctuation with the original loss distribution.

The number of cycles to failure $N_f$ is estimated by the Bayerer lifetime model, presented earlier, is used:

$$N_{f(l,s)} = A \Delta T_{j(l,s)}^{\beta_1} exp\left(\frac{\beta_2}{T_{jm(l,s)} + 273}\right) t_{on(l,s)}^{\beta_3} I^{\beta_4} V^{\beta_5} D^{\beta_6}. \tag{3.20}$$

This equation can be applied to both time constants and is used to quantify the wear-out bond wire lift-off due to thermo-mechanical stress in the the power device bond wire. In addition, long-term analysis is carried out by limiting thermal cycles in the range of 1-15s, according to the parameters defined in Tab. 3.

Since (3.20) is defined to $t_{on}$ from 1-15s, the estimated number of cycles for short-term analysis $N_{f(s)}$ may be incorrect. (TECHNOLOGIES, 2010) shows the dependence of $N_{f(s)} = \mathrm{f}(t_{on(s)})$, given by:

$$\frac{N_{f(s)}(t_{on(s)})}{N_{f(s)}(1.5s)} = \left(\frac{t_{on(s)}}{1.5s}\right)^{-0.3}, \; 0.1s < t_{on(s)} < 60s. \tag{3.21}$$

Thus, $N_{f(s)}$ is calculated correctly for selected $t_{on(s)}$ in the range of 0.1-60s (in this case, 1.5s) and the correction for $t_{on(s)}$=1/120s can be performed using (3.21). Although the heating time for the real application is not in the range of (3.21), it is the best approach found in the literature.

Table 3 – Parameters and limits for the calculation of $N_f$ based on the Bayerer Model after the correction (REIGOSA, 2014).

| Parameter | Label | Limits | Coef. | Value |
|---|---|---|---|---|
| Technology factor | $A$ | - | - | $9.3410^{14}$ |
| Temp. fluctuation | $\Delta T_j$ | 45-150 °$C$ | $\beta_1$ | -4.416 |
| Min. junction temp. | $T_{j,min}$ | 20-120 °$C$ | $\beta_2$ | 1285 |
| Cycling period | $t_{on}$ | 0.1-60s | $\beta_3$ | -0.463 |
| Current per bond foot | $I$ | 3-23A | $\beta_4$ | -0.716 |
| Blocking voltage | $V$ | 6-33V | $\beta_5$ | -0.761 |
| Bond wire diameter | $D$ | 75-500$\mu$m | $\beta_6$ | -0.5 |

### 3.3.3 Lifetime Consumption Evaluation

The total 1-year lifetime consumption ($LC$) is a cumulative sum of the thermal cycle contributions due to the grid fundamental frequency (short-term) and climatic variations (long-term), represented by (3.22). As the grid frequency is 60 Hz and the data is sampled at 1 second, there are 60 cycles per sample to be counted in the short-term contribution.

$$LC = \sum_{k} \left( \frac{\overbrace{1}^{long-term}}{N_{f(l)_k}} + \frac{\overbrace{60}^{short-term}}{N_{f(s)_k}} \right). \tag{3.22}$$

## 3.4 Monte Carlo Reliability Analysis

The total LC for one year is considered under a specific profile and it is understood that all the power devices will failure at the same time. However, depending on the manufacturing process and thermal stresses, the power devices can fail at different times due to uncertainties in the device parameter variations and the statistical properties of the applied lifetime model (REIGOSA, 2014). Thus, the insertion of random variations in the power devices parameters is a way of approaching their actual operating conditions. Therefore, a statistical analysis based on Monte-Carlo simulation is proposed, as illustrated in Fig. 22 (SHEN et al., 2016; SANGWONGWANICH et al., 2018; ANURAG; YANG; BLAABJERG, 2015b; REIGOSA et al., 2016).

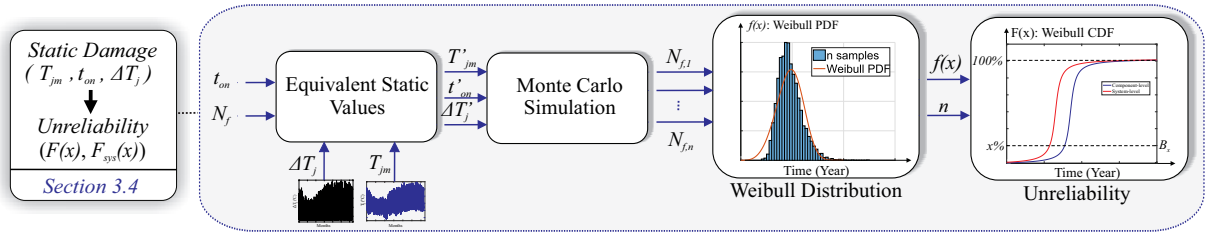


Figure 22 – Flowchart of the Monte Carlo reliability analysis.

In the first step, the stochastic and dynamic parameters of $\Delta T_j$, $t_{on}$ and $T_{jm}$ have to be converted into equivalent deterministic and static ones, referred as $\Delta T_j^{'}$, $t_{on}^{'}$ and $T_{jm}^{'}$ (SANGWONGWANICH et al., 2018). The main goal is obtaining the parameters which provide the same $LC$ calculated in (3.22). Reference (SANGWONGWANICH et al., 2018) suggests taking $T_{jm}^{'}$ as the mean value of the junction temperature $T_j$ and $t_{on}^{'} = 1/(2f_n)$ to reduce the number of degrees of freedom, since it is the most stressful heating time in the power devices.

By setting $t_{on}^{'}$, it is possible to calculate the number of cycles of the device per year as $NC^{'} = 365 \times 24 \times 60 \times 60 \times 60$. In addition, with the $LC$ value, it is possible to

determine $N_f^{'}$ by means of the Palmgren-Miner's rule:

$$LC = \frac{NC^{'}}{N_f^{'}}. \tag{3.23}$$

Finally, the equivalent static junction temperature fluctuation $\Delta T_j^{'}$ is obtained by applying (3.20) using the defined deterministic parameters:

$$\Delta T_j^{'} = \sqrt[\beta_1]{\frac{N_f^{'}}{kexp\left(\frac{\beta_2}{T_{jm}^{'}+273}\right) t_{on}^{'\beta_3}}}, \tag{3.24}$$

where $k = AI^{\beta_4}V^{\beta_5}D^{\beta_6}$. Once the equivalent static values are obtained, a variation of 5% is applied in these parameters and in all the coefficients of Tab. 3. Then, the Monte-Carlo simulation is performed with a population of 10000 samples.

The output values from the Monte-Carlo simulation can be arranged in a histogram. The distribution of the power devices lifetime generally follows the Weibull function $f(x)$ (ZHOU et al., 2016), given by:

$$f(x) = \frac{\beta}{\eta^{\beta}} x^{\beta-1} exp\left[-\left(\frac{x}{\eta}\right)^{\beta}\right], \tag{3.25}$$

where $\eta$ is the scale parameter, $\beta$ is the shape parameter and $x$ is the operation time (SANGWONGWANICH et al., 2018). All these parameters are estimated for a maximum likelihood with the Weibull distribution. Therefore, it is possible to fit the Probability Density Function (PDF) $f(x)$ in the histogram generated with the $n = 10000$ samples (REIGOSA et al., 2016).

Finally, the reliability of one power device can be evaluated by considering the Cumulative Density Function (CDF) $F(x)$ of the Weibull distribution, given by the PDF area, as:

$$F(x) = \int_0^x f(x)dx. \tag{3.26}$$

$F(x)$ is called unreliability function. In addition, from $F(x)$ it is possible to obtain the lifetime $B_x$, which refers to the time when $x$% of samples have failed (REIGOSA et al., 2016). $B_{10}$ is the common reliability metric used by manufacturers and project engineers.

With the Monte-Carlo analysis, the failure of one power device can occur at a different time than another. However, the system fails when any device fails (redundancy

is being neglected in this case). Therefore, the unreliability function of the three-phase system $F_{sys}$ can be obtained by,

$$F_{sys}(x) = 1 - \prod_{i=1}^{6}(1 - F_i(x)). \tag{3.27}$$

Due to the uniform distribution of power between the inverter phases, all devices converge to the same cumulative density function $F_i(x)$. Then, it is possible to simplify (3.27) by,

$$F_{sys}(x) = 1 - (1 - F(x))^6. \tag{3.28}$$

# 4 Results and Discussion

The motivation of this chapter is to provide the lifetime evaluation of switching devices based on long-term and short-term realistic thermal stress. The final goal of this work is to evaluate the trade-off between a possible reduction of the lifetime of the PV inverter compensating reactive power and the advantages and flexibility of its new functionality.

## 4.1 Case Study

The $Q$ injection impact is evaluated by means of the simulation of a 8 kVA three-phase PV inverter, whose parameters are presented in Tab. 4.

Table 4 – Parameters of the PV system.

| Parameter | Label | Value |
|---|---|---|
| Rated power | $S$ | 8kVA |
| Rated rms grid voltage | $V_g$ | 380V |
| Dc-link voltage | $v_{dc}$ | 630V |
| Nominal grid frequency | $f_n$ | 60Hz |
| Dc-link capacitor | $C_{dc}$ | 1mF |
| Filter inductance | $L_g$ | 0.2mH |
| Filter inductance | $L_f$ | 0.2mH |
| Filter capacitance | $C_f$ | 15.6$\mu$F |
| Filter damping resistor | $r_d$ | 0.4$\Omega$ |
| Switching frequency | $f_{sw}$ | 12kHz |

The parameters of the controllers are shown in Tab. 5. The proportional integral controllers are discretized by Tustin method, with sampling frequency equal to the switching frequency.

Two scenarios are evaluated:

1. Component and system-level lifetime evaluation for the PV inverter injecting only active power, according to the conditions of the mission profile;

2. Component and system-level lifetime evaluation for the PV inverter injecting active and reactive power, according to the conditions of the mission profile.

Table 5 – Controllers gains.

| Controllers gains | | Value |
|---|---|---|
| PLL | $k_{i1}$ | 50.895 |
| | $k_{p1}$ | 0.572 |
| Inner loop | $k_{p,i}$ | 1.531 |
| | $k_{i,i}$ | 14.432 |
| $Q$ loop | $k_{i,Q}$ | -0.405 |
| | $k_{p,Q}$ | -0.0005 |
| $v_{dc}^2$ loop | $k_{i,bus}$ | 14.212 |
| | $k_{p,bus}$ | 0.226 |

## 4.2 Total LC based on Mission Profile

Before performing lifetime analysis of the semiconductor devices, Fig. 23 shows simulated diode and IGBT switching and conduction losses for varying $P$ and $Q$ injection conditions. As expected, the total power losses are directly affected by the $Q$ compensation.

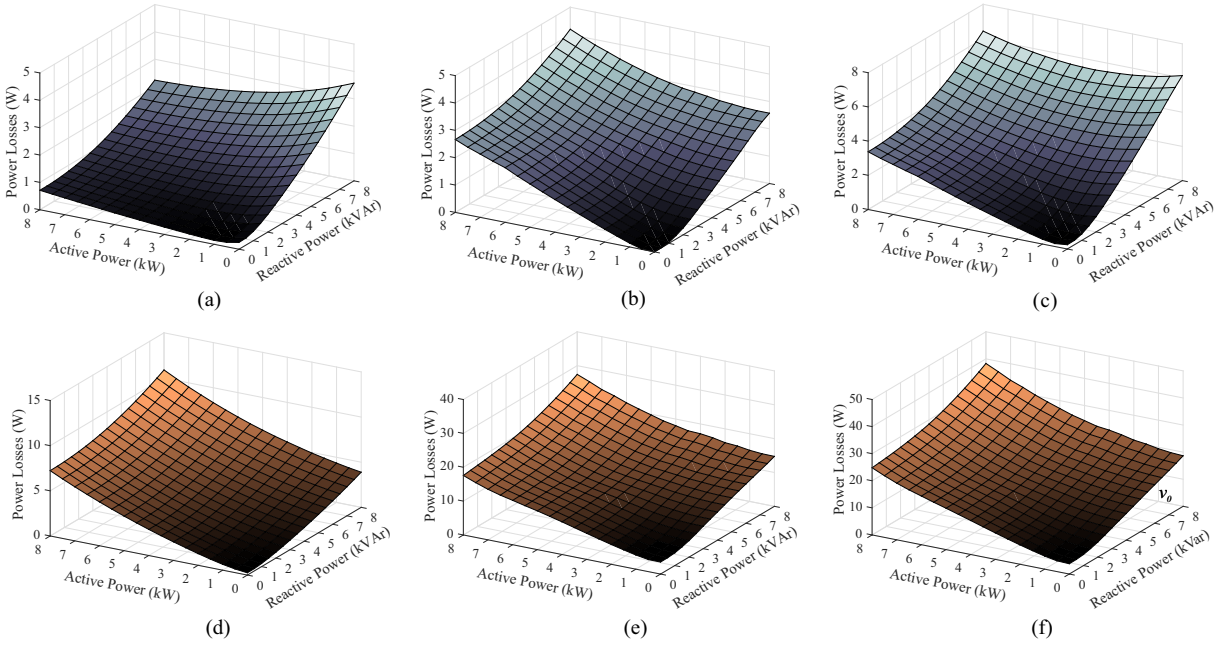


Figure 23 – Power losses in the semiconductors devices considering different injections of active and reactive power. Diode: (a) conduction losses, (b) switching losses, (c) total losses. IGBT: (d) conduction losses, (e) switching losses, (f) total losses.

According to Fig. 23 (a), the diode conduction losses when the PV inverter injects only $Q$ ($\theta = \pm 90°$) are approximately 5 times higher than the power losses with only $P$ injection ($\theta = 0$). Fig. 23 (d) shows that the IGBT power conduction losses behavior is opposite, considering the points analyzed above. Thus, these power losses are twice as low as the power losses caused by $P$ injection.

The diode and IGBT switching power losses have the same behavior: they are higher for high values of $S$ injection. This can be explained by the increase in current amplitude. However, note that for rated apparent power injection, i.e., keeping the current amplitude constant, the IGBT and diode switching power losses suffer little fluctuation with $\theta$ variation, as discussed in previous chapter. The combined injection of $Q$ and $P$ increases conduction and switching power losses, since it is directly related to the current flowing in the power devices.

Fig. 23 (c) and (f) show the total power losses of the diode and IGBT, respectively. For the conditions of $Q = 8k$VAr and $P = 8k$W, the IGBT total power losses are 6 times greater than the diode total power losses, which causes the extra heating of these components. At this point of the operation, the system apparent power is 41.4% higher than the operation without reactive power injection. For a safer and more reliable operation, strategies to limit $S$ to its curtailment value can be adopted. However, this work focuses on evaluating the damage caused in the semiconductor devices due to the injection of the reactive power requested by the load.

The junction temperature of the power devices is a consequence of the power losses. Thus, it is observed that the $Q$ injection impacts the PV inverter through the junction temperature profile $T_j$, as shown in Fig. 24 (a) and (c), for the IGBT and diode, respectively. In addition, the cycle amplitude $\Delta T_j$ is also affected, as shown in Fig. 24 (b) and (d) for the IGBT and diode. $T_j$ and $\Delta T_j$ for the $Q$ compensation case are always higher, compared to the case without reactive power compensation.

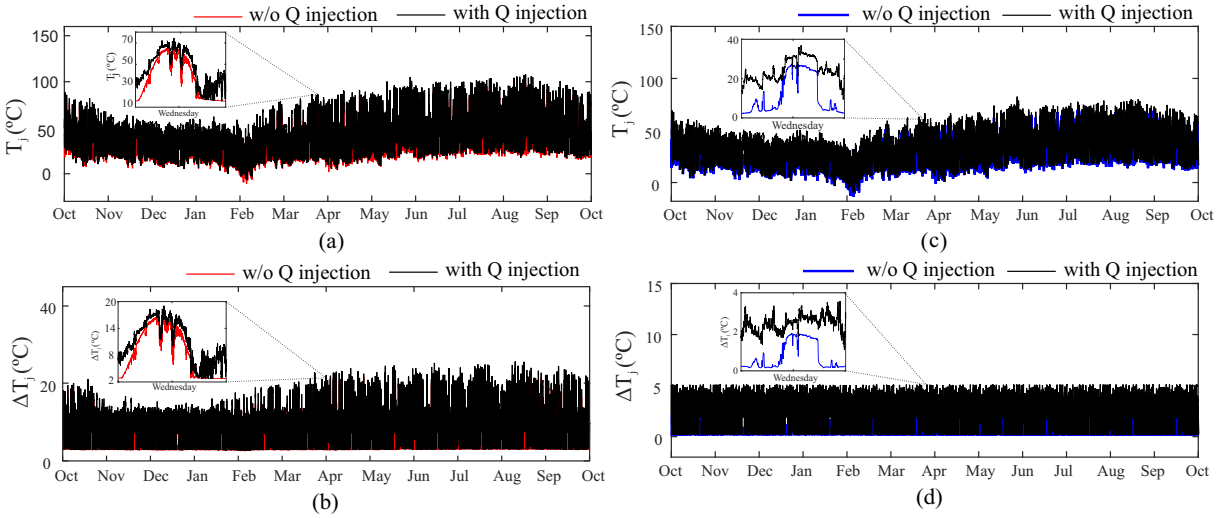


Figure 24 – (a) IGBT junction temperature behavior with and without $Q$ injection. (b) IGBT junction temperature fluctuation with and without $Q$ injection. (c) Diode junction temperature behavior with and without $Q$ injection. (d) Diode junction temperature fluctuation with and without $Q$ injection.

It is interesting to analyze the device that is being more thermally stressed. From the results observed in Fig. 23 and 24, the IGBT showed higher power losses, junction

temperature and junction temperature variation compared to the diode. Therefore, the IGBT is expected to be the most critical component of the system and, due to the reasons present above, it was selected to evaluate the system lifetime.

The power devices of the PV inverter injecting reactive power are subject to higher thermal stresses over a traditional PV inverter. This extra stress can cause more damage to the power devices and impact their reliability and lifetime. The one year thermal loading distribution obtained for the power modules under the mission profile conditions was used as an input to calculate the accumulated damage per year. These results are shown in Tab. 6. It can be noticed that the reactive power compensation according to the load requirements causes greater damage to the devices (0.1377), when compared to the base case, i.e., without $Q$ compensation (0.0461).

Table 6 – Lifetime consumption due $T_a$, $G$ and $Q$ profiles, based on the Palmgren-Miner's rule (3.22) for one year.

| Time Constant | Lifetime Consumption (LC) | |
|---|---|---|
| | w/o $Q$ injection | with $Q$ injection |
| Long-term | 0.000004355 | 0.000001347 |
| Short-term | 0.0461 | 0.1377 |
| Total | 0.0461 | 0.1377 |

It is important to point out that a filtering of the rainflow algorithm output data for the long-term analysis was done aiming to select only the $t_{on}$ within the Bayerer model validity range. For a dynamic and realistic analysis, all parameters of the system under study must be modeled by means of probability distribution functions. Therefore, the lifetime distribution $f(x)$ is obtained for two cases: with $Q$ injection and without $Q$ injection, as shown in Fig. 25 (a).

The results in Fig. 25 demonstrate that the injection of $Q$ strongly impacts the lifetime distribution of the power module. With $Q$ injection, there is a higher concentration of the distribution $f(x)$ in the range of 5-10 lifetime years. On the other hand, without $Q$ injection, a considerable distribution is present in the range of 15-30 lifetime years.

The reliability of the power module can be evaluated by considering the CDF of the Weibull distribution. However, to evaluate the lifetime of the entire system, it is necessary to consider the interaction between the reliability of each component.

The unreliability functions of one component (i.e. component-level) for the cases without and with $Q$ injection are indicated in Fig. 26 (a) and (b), respectively. The $B_{10}$ lifetime of the power device for the first case is 14.5 years. On the other hand, for the second one, $B_{10}$ lifetime of the power device declined to 5 years, which reduces power devices lifetime by 65.5%.

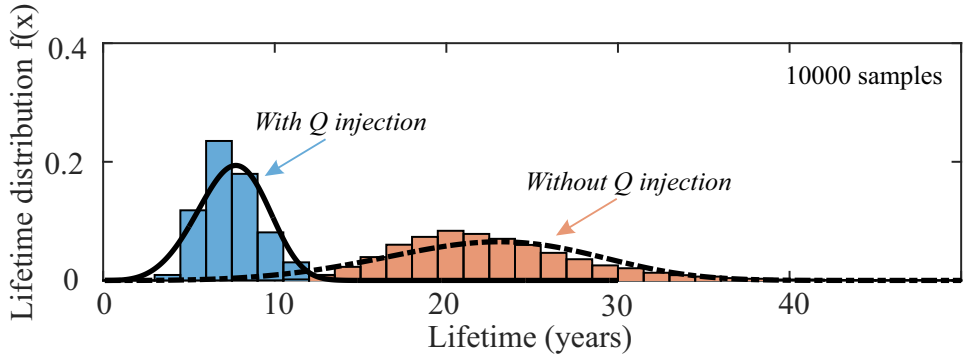


Figure 25 – Damage distribution analysis of the power module with and without Q injection. Unreliability function of the PV inverter (b) without $Q$ compensation; (c) with $Q$ compensation.

Fig. 26 (a) and (b) show the system-level unreliability function without and with $Q$ injection, respectively.

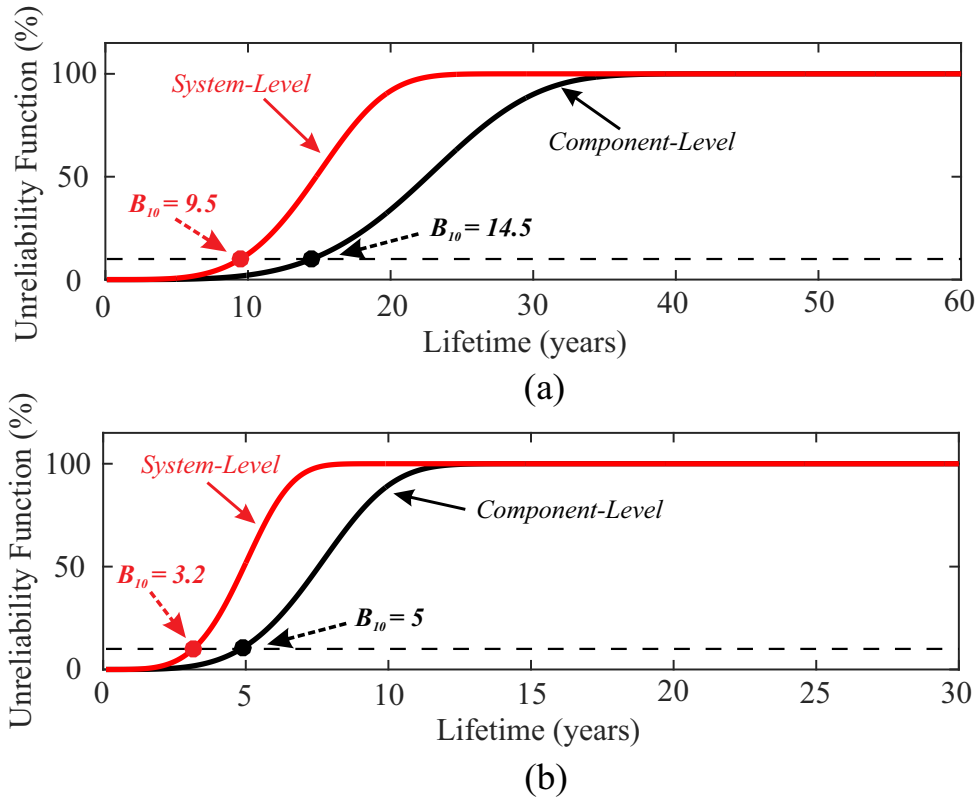


Figure 26 – Unreliability function of the PV inverter (a) without $Q$ compensation; (b) with $Q$ compensation.

It can be seen that the system-level $B_{10}$ differs significantly from the component-level lifetime, for both cases. The system level $B_{10}$ lifetime of the PV inverter, considering the mission profile in Denmark, is 9.5 years if the reactive power injection is not considered. Considering it, the system level $B_{10}$ lifetime declines to 3.2 years. This means that, considering the reactive power injection, the PV inverter has a lifetime reduction of 66.3%

when compared to the PV inverter without $Q$ injection.

Therefore, the results demonstrate that the reactive power injection has a strong impact on the lifetime prediction of the PV inverter. Therefore, it should be taken into consideration in the evaluation of the PV inverter lifetime.

# 5 Conclusion

The lifetime impact on a multifunctional PV inverter compensating reactive power was provided in this work. It was verified that the reactive power injection implies in the additional increase in the junction temperature and consequently in the thermal stress of the power devices. Thus, the Monte-Carlo analysis reveals that the lifetime consumption of the PV inverters decreases considerably with the reactive power injection, according to the $Q$ profile. As a result, it was observed that the multifunctional PV inverter failure time is almost 3 times lower, compared to the traditional PV inverter.

One-year simulations with mission profile data were conducted to analyze the lifetime effects of PV inverters with reactive power compensation. The results of this work were obtained for the location of the PV plant in Denmark and the reactive power profile requirement by a food industry. For installation in another industry or other country, the PV inverters lifetime will differ from those presented. Therefore, it is important to consider these aspects in the PV inverters reliability design.

The PV inverter with reactive power support can improve the quality of the power system as it reduces power losses in the distribution and transmission lines, provides voltage regulation and aids in events such as transient voltage sags. However, despite the great attractiveness of the multifunctional PV inverter, a considerable reduction in the PV inverters lifetime is observed when providing this new functionality.

There is a trade-off between the advantages and impacts of reactive power injection. In summary, some obstacles related to the reliability and lifetime of the PV inverter still have to be overcome to make it even more attractive, in order to aid in making decision.

## 5.1 Final Considerations

It is difficult to precisely estimate the lifetime of a power device. It involves several other factors that are beyond the scope of this work. For example, in the lifetime calculation, only the thermal cycles induced by the mission profile in the range of 0.1-60s are considered. Even with high oscillations in min-hour time constants present in the reactive power profile, any long-term cycle outside this range was ignored due to the lifetime model limitation. In order to mitigate these errors, all analyzes were presented using the same methodology, by means of comparation of the estimated system lifetime with and without $Q$ injection.

The current grid code requirements request reactive power injection during voltage sag events ranged at sec-min intervals. In this context, the PV inverter may not be severely damaged. In other words, only a control update on the software firmware is required to

convert the conventional PV inverter into a multifunctional operation.

Unfortunately, with a continuous $Q$ injection as a consequence of low PF (i.e. reactive power profile), a hardware upgrade is required. Therefore, a PoF-oriented design of the components must be performed in order to ensure a highly reliable operation of the PV multifunctional inverter. The choice of new IGBT module technologies, made from silicon carbide (SiC) for example, can be an interesting option. Another alternative is improving the cooling of the power modules, since their average temperature increases with the reactive power injection.

## 5.2 Continuity Proposals

For future developments of this research, the following studies may be suggested:

1. Evaluate the lifetime of dc-link capacitors under mission profile conditions;
2. Take into account the dynamic saturation of the PV inverter;
3. Propose a junction temperature control, i.e., if the junction temperature exceeds a certain range, the PV inverter should disable the $Q$ injection functionality. In this way, it will always operate under controlled thermal stress, improving reliability and lifetime;
4. Estimate the cost of reactive power compensation in terms of energy.

# References

AGENCY, I. E. *Renewables 2017 : Key Findings*. 2018. Disponível em: <https://www.iea.org/publications/renewables2017.> 19

ALMEIDA, P. Machado de. *Modelagem e Controle de Conversores Estáticos Fonte de Tensão Utilizados em Sistemas de Geração Fotovoltaicos Conectados à Rede Elétrica de Distribuição*. Dissertação (Mestrado) — Universidade Federal de Juiz de Fora, 2011. 20, 25, 28

ANDRADE, E. G. de et al. Power losses in photovoltaic inverter components due to reactive power injection. In: *2016 12th IEEE Int. Conf. on Ind. Applications (INDUSCON)*. [S.l.: s.n.], 2016. p. 1–7. 20

ANDRESEN, M. et al. Thermal stress comparison in modular power converter topologies for smart transformers in the electrical distribution system. In: *2015 17th European Conference on Power Electronics and Applications (EPE'15 ECCE-Europe)*. [S.l.: s.n.], 2015. p. 1–10. 44

ANURAG, A.; YANG, Y.; BLAABJERG, F. Reliability analysis of single-phase pv inverters with reactive power injection at night considering mission profiles. In: *2015 IEEE Energy Conversion Congress and Exposition (ECCE)*. [S.l.: s.n.], 2015. p. 2132–2139. ISSN 2329-3721. 22, 24

ANURAG, A.; YANG, Y.; BLAABJERG, F. Thermal performance and reliability analysis of single-phase pv inverters with reactive power injection outside feed-in operating hours. *IEEE Journal of Emerging and Selected Topics in Power Electronics*, v. 3, n. 4, p. 870–880, Dec 2015. ISSN 2168-6777. 20, 39, 49

BAYERER, R. et al. Model for power cycling lifetime of igbt modules - various factors influencing lifetime. In: *5th Int. Conf. on Integrated Power Electronics Systems*. [S.l.: s.n.], 2008. p. 1–6. 32, 33

BIERHOFF, M. H.; FUCHS, F. W. Semiconductor losses in voltage source and current source igbt converters based on analytical derivation. In: *2004 IEEE 35th Annual Power Electronics Specialists Conference (IEEE Cat. No.04CH37551)*. [S.l.: s.n.], 2004. v. 4, p. 2836–2842 Vol.4. ISSN 0275-9306. 37, 38

CASANELLAS, F. Losses in pwm inverters using igbts. *IEE Proceedings - Electric Power Applications*, v. 141, n. 5, p. 235–239, Sept 1994. ISSN 1350-2352. 36, 37, 39, 67, 69

CHUNG, S.-K. A phase tracking system for three phase utility interface inverters. *IEEE Transactions on Power Electronics*, v. 15, n. 3, p. 431–438, May 2000. ISSN 0885-8993. 27, 32

FERREIRA, V. N. et al. Igbt power modules lifetime in 2-level pv-inverters under harsh environmental conditions. In: *2017 IEEE 8th Int. Symposium on Power Electronics for Distributed Generation Systems (PEDG)*. [S.l.: s.n.], 2017. p. 1–7. 22, 33

GANDHI, O. et al. Reactive power cost from pv inverters considering inverter lifetime assessment. *IEEE Transactions on Sustainable Energy*, p. 1–1, 2018. ISSN 1949-3029. 22

GANGOPADHYAY, U.; JANA, S.; DAS, S. State of art of solar photovoltaic technology. *Journal of Energy*, v. 764132, 04 2013. 19

GAO, Z. et al. An overview of pv system. In: *2016 IEEE International Conference on Mechatronics and Automation*. [S.l.: s.n.], 2016. p. 587–592. ISSN 2152-744X. 19

GOLESTAN, S.; GUERRERO, J. M.; VASQUEZ, J. C. Three-phase plls: A review of recent advances. *IEEE Trans. on Power Electronics*, v. 32, n. 3, p. 1894–1907, March 2017. ISSN 0885-8993. 26

GOMES, C. C.; CUPERTINO, A. F.; PEREIRA, H. A. Damping techniques for grid-connected voltage source converters based on lcl filter: An overview. *Renewable and Sustainable Energy Reviews*, v. 81, p. 116 – 135, 2018. ISSN 1364-0321. Disponível em: <http://www.sciencedirect.com/science/article/pii/S1364032117311206>. 25

GOPIREDDY, L. R. et al. Rainflow algorithm-based lifetime estimation of power semiconductors in utility applications. *IEEE Transactions on Industry Applications*, v. 51, n. 4, p. 3368–3375, July 2015. ISSN 0093-9994. 46

HAVA, A. M.; KERKMAN, R. J.; LIPO, T. A. Simple analytical and graphical methods for carrier-based pwm-vsi drives. *IEEE Transactions on Power Electronics*, v. 14, n. 1, p. 49–61, Jan 1999. ISSN 0885-8993. 29

HELD, M. et al. Fast power cycling test of igbt modules in traction application. In: *Proceedings of Second International Conference on Power Electronics and Drive Systems*. [S.l.: s.n.], 1997. v. 1, p. 425–430 vol.1. 32, 33

INFINEON. *Transient Thermal Measurements and Thermal Equivalent Circuit Models*. 2015. Disponível em: <https://www.infineon.com/dgdl/Infineon-AN2015_10_Thermal_equivalent_circuit_models-AN-v01_00-EN.pdf?fileId=db3a30431a5c32f2011aa65358394dd2>. 47

JäGER-WALDAU, A. *PV Status Report 2017*. 2017. Disponível em: <https://ec.europa.eu/jrc/sites/jrcsh/files/kjna28817enn.pdf>. 19, 20

KAPLAR, R. et al. Pv inverter performance and reliability: What is the role of the igbt? In: *2011 37th IEEE Photovoltaic Specialists Conference*. [S.l.: s.n.], 2011. p. 001842–001847. ISSN 0160-8371. 22

LIBO, W.; ZHENGMING, Z.; JIANZHENG, L. A single-stage three-phase grid-connected photovoltaic system with modified mppt method and reactive power compensation. *IEEE Trans. on Energy Conversion*, v. 22, n. 4, p. 881–886, Dec 2007. ISSN 0885-8969. 20

LISERRE, M.; BLAABJERG, F.; HANSEN, S. Design and control of an lcl-filter-based three-phase active rectifier. *IEEE Transactions on Industry Applications*, v. 41, n. 5, p. 1281–1291, Sept 2005. ISSN 0093-9994. 24

LIU, L. et al. Reactive power compensation and optimization strategy for grid-interactive cascaded photovoltaic systems. *IEEE Trans. on Power Electronics*, v. 30, n. 1, p. 188–202, Jan 2015. ISSN 0885-8993. 20

MA, K. *Power Electronics for the Next Generation Wind Turbine System*. 1. ed. Springer International Publishing, 2015. (Research Topics in Wind Energy 5). ISBN 978-3-319-21247-0,978-3-319-21248-7. Disponível em: <http://gen.lib.rus.ec/book/index.php?md5=60278F388EA42D2BCF3821E7D57F55E6>. 44

MA, K.; BLAABJERG, F. Reliability-cost models for the power switching devices of wind power converters. In: *2012 3rd IEEE Int. Symposium on Power Electronics for Distributed Generation Systems (PEDG)*. [S.l.: s.n.], 2012. p. 820–827. ISSN 2329-5759. 43, 46, 47, 48

MA, K. et al. Thermal loading and lifetime estimation for power device considering mission profiles in wind power converter. *IEEE Trans. on Power Electronics*, v. 30, n. 2, p. 590–602, Feb 2015. ISSN 0885-8993. 8, 43, 45, 46, 48

MANSON, S. S. *Thermal Stress and Low Cycle Fatigue*. [S.l.]: McGraw-Hill, 1966. 33

MAYER, J. N. *Current and Future Cost of Photovoltaics*. 2015. Disponível em: <https://www.ise.fraunhofer.de/content/dam/ise/de/documents/publications/studies/AgoraEnergiewende_Current_and_Future_Cost_of_PV_Feb2015_web.pdf>. 19

MIL-HDBK-217E. *Military Handbook: Reliability Prediction of Electronic Equipment*. [S.l.]: Department of Defense - USA, 1991. 32

MURAY, C. J.; DAVOUDI, A.; CHAPMAN, P. L. Reliability analysis for single-phase photovoltaic inverters with reactive power support. In: *2011 IEEE Power and Energy Conf. at Illinois*. [S.l.: s.n.], 2011. p. 1–6. 22

NORRIS, K. C.; LANDZBERG, A. H. Reliability of controlled collapse interconnections. *IBM Journal of Research and Development*, v. 13, n. 3, p. 266–271, May 1969. ISSN 0018-8646. 32, 33

PEñA-ALZOLA, R. et al. Lcl-filter design for robust active damping in grid-connected converters. *IEEE Transactions on Industrial Informatics*, v. 10, n. 4, p. 2192–2203, Nov 2014. ISSN 1551-3203. 25

PEREIRA, H. A. et al. Single-phase multifunctional inverter with dynamic saturation scheme for partial compensation of reactive power and harmonics. In: *2015 17th European Conference on Power Electronics and Applications (EPE'15 ECCE-Europe)*. [S.l.: s.n.], 2015. p. 1–10. 20

PINTO, A.; ZILLES, R. Reactive power excess charging in grid-connected pv systems in brazil. *Renewable Energy*, v. 62, p. 47 – 52, 2014. ISSN 0960-1481. 21

REIGOSA, P. D. *Smart Derating of Switching Devices for Designing More Reliable PV Inverters*. Dissertação (Mestrado) — Aalborg University, 2014. 10, 20, 22, 41, 48, 49

REIGOSA, P. D. et al. Prediction of bond wire fatigue of igbts in a pv inverter under a long-term operation. *IEEE Transactions on Power Electronics*, v. 31, n. 10, p. 7171–7182, Oct 2016. ISSN 0885-8993. 32, 49, 50

REN21. *Renewables 2018: Global Status Report*. 2018. Disponível em: <http://www.ren21.net/wp-content/uploads/2018/06/17-8652_GSR2018_FullReport_web_final_.pdf.> 8, 19

RODRIGUEZ, P. et al. Decoupled double synchronous reference frame pll for power converters control. *IEEE Transactions on Power Electronics*, v. 22, n. 2, p. 584–592, March 2007. ISSN 0885-8993. 25

SANGWONGWANICH, A.; LIIVIK, E.; BLAABJERG, F. Photovoltaic module characteristic influence on reliability of micro-inverters. In: *2018 IEEE 12th International Conference on Compatibility, Power Electronics and Power Engineering (CPE-POWERENG 2018)*. [S.l.: s.n.], 2018. p. 1–6. 22

SANGWONGWANICH, A. et al. Lifetime evaluation of grid-connected pv inverters considering panel degradation rates and installation sites. *IEEE Trans. on Power Electronics*, v. 33, n. 2, p. 1225–1236, Feb 2018. ISSN 0885-8993. 19, 20, 43, 46, 49, 50

SARKAR, M. N. I.; MEEGAHAPOLA, L. G.; DATTA, M. Reactive power management in renewable rich power grids: A review of grid-codes, renewable generators, support devices, control strategies and optimization algorithms. *IEEE Access*, p. 1–1, 2018. 21

SHEN, Y. et al. Mission profile based sizing of igbt chip area for pv inverter applications. In: *2016 IEEE 7th Int. Symp. on Power Electronics for Distributed Generation Systems (PEDG)*. [S.l.: s.n.], 2016. p. 1–8. 49

TECHNOLOGIES, I. *Technical Information IGBT modules - Use of Power Cycling curves for IGBT 4*. 2010. Disponível em: <http://song-shan.com/en/upload/file/20140413/122019_Use%20of%20Power%20Cycling%20Curves%20for%20IGBT4%20.pdf.> 48

TEIXEIRA, D. *Controle Vetorial do Motor de Indução Operando na Região de Enfraquecimento de Campo*. 2010. Monografia (Bacharel em Engenharia Elétrica),UFV (Universidade Federal de Viçosa), Viçosa, Brasil. 25

VILLALVA, M. G.; GAZOLI, J. R.; FILHO, E. R. Comprehensive approach to modeling and simulation of photovoltaic arrays. *IEEE Trans. on Power Electronics*, v. 24, n. 5, p. 1198–1208, May 2009. ISSN 0885-8993. 44

WANG, H. et al. Transitioning to physics-of-failure as a reliability driver in power electronics. *IEEE Journal of Emerging and Selected Topics in Power Electronics*, v. 2, n. 1, p. 97–114, March 2014. ISSN 2168-6777. 30, 31, 32

XAVIER, L. S.; CUPERTINO, A. F.; PEREIRA, H. A. Ancillary services provided by photovoltaic inverters: Single and three phase control strategies. *Computers and Electrical Engineering*, 2018. ISSN 0045-7906. Disponível em: <http://www.sciencedirect.com/science/article/pii/S0045790617303403>. 25, 29, 34

XIONG, Y. et al. Prognostic and warning system for power-electronic modules in electric, hybrid electric, and fuel-cell vehicles. *IEEE Trans. on Industrial Electronics*, v. 55, n. 6, p. 2268–2276, June 2008. ISSN 0278-0046. 41

YANG, Y.; SANGWONGWANICH, A.; BLAABJERG, F. Design for reliability of power electronics for grid-connected photovoltaic systems. *CPSS Trans. on Power Electronics and Applications*, v. 1, n. 1, p. 92–103, Dec 2016. ISSN 2475-742X. 31, 43, 46

ZENG, Z. et al. Objective-oriented power quality compensation of multifunctional grid-tied inverters and its application in microgrids. *IEEE Transactions on Power Electronics*, v. 30, n. 3, p. 1255–1265, March 2015. ISSN 0885-8993. 20

ZHANG, J. et al. Thermal control method based on reactive circulating current for anti-condensation of wind power converter under wind speed variations. In: *2014 International Power Electronics and Application Conference and Exposition*. [S.l.: s.n.], 2014. p. 152–156. 22

ZHOU, D. et al. System-level reliability assessment of power stage in fuel cell application. In: *2016 IEEE Energy Conversion Congress and Exposition (ECCE)*. [S.l.: s.n.], 2016. p. 1–8. 50

ZOU, Z.; WANG, Z.; CHENG, M. Modeling, analysis, and design of multifunction grid-interfaced inverters with output lcl filter. *IEEE Trans. on Power Electronics*, v. 29, n. 7, p. 3830–3839, July 2014. ISSN 0885-8993. 24

# APPENDIX A – Switching Power Losses Modeling

The study of conduction and switching power losses in semiconductor devices is an indicative of the thermal stress to which they are subjected. Thus, a greater detail in obtaining the mathematical models of switching power losses when the PV inverter injects reactive power is fundamental for the understanding of this work.

## A.1 IGBT Switching Power Losses Modeling

The switching power losses are accumulated when the IGBT and diode are turned on and when they are turned off. The energy $E_{i,on}$ and $E_{i,off}$ required to perform the device switching are usually presented as graphs in the datasheets provided by the manufacturer. In addition, this energy can be calculated from the typical characteristic of power devices current and voltage.

### A.1.1 Turn on Switching Power Losses

Fig. 27(a) show this typical curve and Fig. 27(b) shows the linear approximation performed to make the calculations feasible.

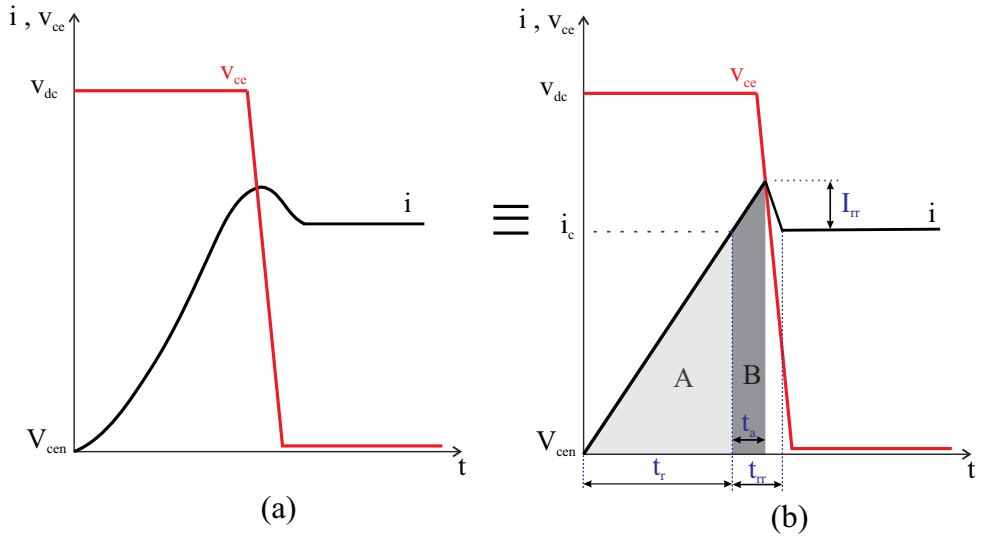


Figure 27 – (a) Typical IGBT turn on curve. (b) Linearized approximation.

The total instantaneous energy $E_{i,on}$ can be approximated by the areas A and B calculation, as highlighted in Fig. 27(b). Thus, $E_{iA,on}$ is obtained by the dc-link $v_{dc}$ product

with the current area:

$$E_{iA,on} = \int_0^{t_r} v_{ce} i_c \frac{t}{t_r} dt = \frac{v_{dc} i_c t_r}{2}, \tag{A.1}$$

where $t_r$ is the IGBT current rising time. However, some of the parameters described by (A.1) are not found on datasheets. It is possible to write:

$$t_r = \frac{t_{rn}}{I_{cn}} i_c, \tag{A.2}$$

where $t_{rn}$ is the rated IGBT current rise time and $I_{cn}$ is the rated collector current when $t = t_{rn}$. Both parameters are easily found on datasheets. Applying (A.2) into (A.1):

$$E_{iA,on} = \frac{v_{dc} t_{rn}}{2} \frac{i_c^2}{I_{cn}}. \tag{A.3}$$

The IGBT current has an increase over the nominal current due to the loads stored in the anti-parallel diode. A depletion region is formed and the diode begins to support the voltage. The stored loads disappear by recombination and the collector voltage begins to decrease (region B). The instantaneous energy can be calculated, considering the following approximations found in (CASANELLAS, 1994):

$$I_{rr} \approx \left(0.7 + \frac{0.3 i_c}{I_{cn}}\right) I_{rrn}, \tag{A.4}$$

$$t_{rr} \approx \left(0.8 + \frac{0.2 i_c}{I_{cn}}\right) t_{rrn}, \tag{A.5}$$

where $I_{rr}$ and $t_{rr}$ are defined on Fig. 27(b). $I_{rrn}$ is the diode nominal reverse recovery current and $t_{rrn}$ is the diode nominal reverse recovery time, both found on datasheets. The linear equation describing the region B current behavior is:

$$i_B = \frac{I_{rr} t}{t_{rr}} + i_c, \tag{A.6}$$

where $t_{rr} \approx t_a$, since almost all power losses are generated in the interval $t_a$. Therefore, the region B instantaneous energy is:

$$E_{iB,on} = \int_0^{t_{rr}} v_{dc} i_B dt = v_{dc} \left[ Q_{rrn} \left(0.28 + 0.19 \frac{i_c}{I_{cn}} + 0.03 \left(\frac{i_c}{I_{cn}}\right)^2\right) + i_c \left(0.8 + 0.2 \frac{i_c}{I_{cn}}\right) t_{rrn} \right], \tag{A.7}$$

and $Q_{rrn} = t_{rrn}I_{rrn}/2$ is the nominal reverse diode recovery load. Finally, the total instantaneous energy is:

$$E_{i,on} = E_{iA,on} + E_{iB,on}, \tag{A.8}$$

or,

$$E_{i,on} = v_{dc}\left[\frac{i_c^2 t_{rn}}{2I_{cn}} + Q_{rrn}\left(0.28 + 0.19\frac{i_c}{I_{cn}} + 0.03\left(\frac{i_c}{I_{cn}}\right)^2\right) + i_c\left(0.8 + 0.2\frac{i_c}{I_{cn}}\right)t_{rrn}\right]. \tag{A.9}$$

Once the instantaneous energy is determined, the calculation of the average power according to the switching frequency $f_{sw}$ can be performed as:

$$P_{on,I} = \frac{f_{sw}}{2\pi}\int_0^{\pi} E_{i,on}d\alpha. \tag{A.10}$$

Finally, considering $i_c$ as defined in Chapter 3,

$$P_{on,I} = \frac{f_{sw}v_{dc}}{2\pi}\left[\frac{\pi I_{cm}^2 t_{rn}}{4I_{cn}} + 2Q_{rrn}\left(0.28\pi + 0.38\frac{I_{cm}}{I_{cn}} + 0.015\pi\frac{I_{cm}^2}{I_{cn}^2}\right) + \left(1.6I_{cm} + 0.1\pi\frac{I_{cm}^2}{I_{cn}}\right)t_{rrn}\right]. \tag{A.11}$$

### A.1.2 Turn off Switching Power Losses

Fig. 28(a) show the IGBT turn off typical curve and Fig. 28(b) shows the linear approximation performed to make the calculations feasible.

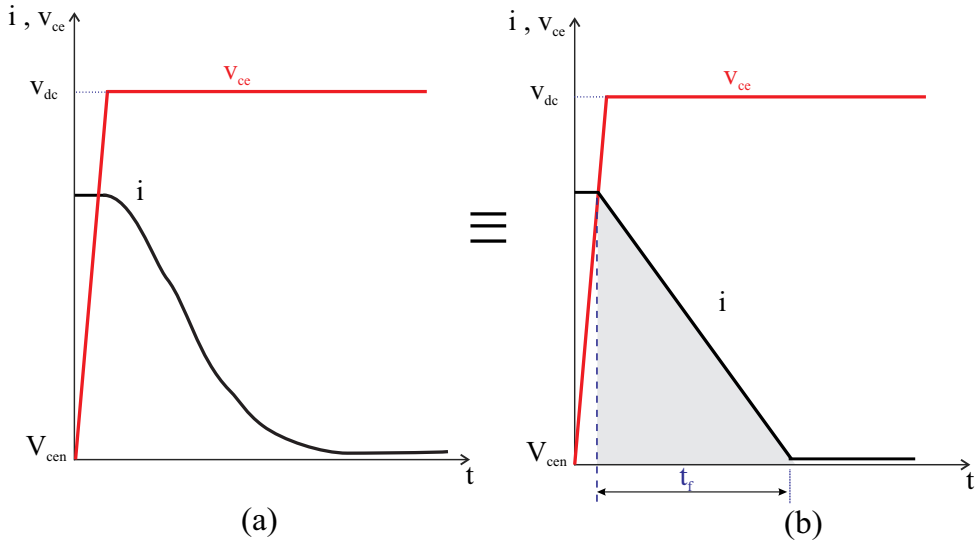


Figure 28 – (a) Typical IGBT turn off curve. (b) Linearized approximation.

According to (CASANELLAS, 1994),

$$t_f \approx \left(\frac{2}{3} + \frac{i_c}{3I_{cn}}\right) t_{fn}, \tag{A.12}$$

where $t_{fn}$ is the rated IGBT current fall time. Analogously,

$$E_{i,off} = \frac{v_{dc} i_c t_f}{2}, \tag{A.13}$$

and,

$$P_{off,I} = \frac{f_{sw} v_{dc} I_{cm} t_{fn}}{2\pi} \left(\frac{2}{3} + \frac{\pi I_{cm}}{12 I_{cn}}\right), \tag{A.14}$$

## A.2 Diode Switching Power Losses Modeling

Diode blocking power losses are proportional to its recovery characteristic. As discussed in Fig. 27, the behavior of the diode reverse recovery current is directly related to the turn off power losses of this component. Besides, the diode turn on power losses are negligible.

The diode blocking losses correspond to a portion of the IGBT switching power losses and, therefore, they are always smaller. As previously calculated,

$$P_{off,D} = \frac{f_{sw} v_{dc} Q_{rrn}}{2\pi} \left[0.28\pi + 0.38\frac{I_{cm}}{I_{cn}}\right]. \tag{A.15}$$